Hybrid Quantum Circuits

Landry Bretheau

Report of Accreditation to Supervise Research

Landry BRETHEAU
QCMX Lab

Laboratoire de Physique de la Matière Condensée (PMC)
CNRS, Ecole Polytechnique, IP Paris

Hybrid Quantum Circuits

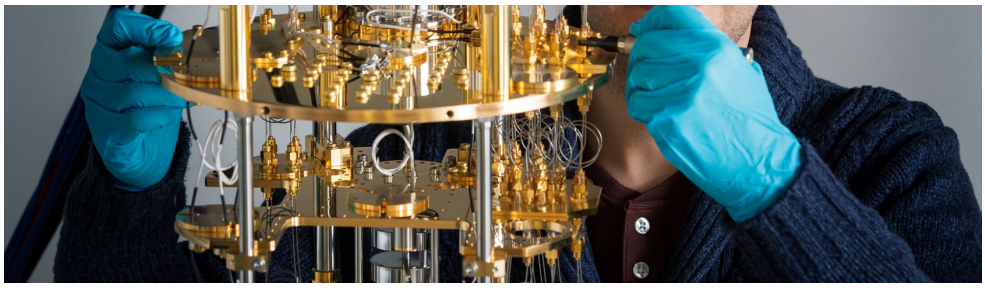

HDR Defense on June 10, 2022

Committee in charge:

Jacqueline BLOCH
Olivier BUISSON
Benoît DOUCOT
Marcelo GOFFMAN
Javier SANCHEZ-YAMAGISHI

Contents

1 Introduction

This manuscript presents the research activity I conducted during the last 13 years, as well as my ongoing and future projects. This research belongs to the dynamic field of quantum mesoscopic physics, which combines basic quantum physics, condensed matter and electronics. Though the experiments I performed are quite diverse, they all involve cleanroom nanofabrication, cryogenic temperatures and low-noise electronic measurements. Writing such a habilitation report is a bit a formal exercise as it is partly redundant with published articles. Therefore, I tried to make it easy to read and I hope the readers will enjoy it and find it interesting.

The manuscript is organized chronologically. Section 2 briefly reports the work I performed as a doctoral student at CEA-Saclay. Using single-atom contacts, I studied the physics of the Andreev bound states, which are the microscopic building block of the Josephson effect. In section 3, I discuss the experiments I made as a post-doctoral associate at ENS. Using superconducting circuits and microwave signals, I could test the back-action of measurement in quantum physics, which induce non-trivial phenomena. Section 4 presents the work I did as a post-doctoral fellow at MIT. I performed experiments with low-dimensional van der Waals materials coupled to superconductors, in order to investigate the intriguing physics that arise in two dimensions. In 2017, I was hired as a permanent researcher at Ecole Polytechnique, where I founded the QCMX Lab together with my colleague Jean-Damien Pillet. In section 5, which is a bit more detailed, I describe the lab construction, some collaborative works and our ongoing research projects on hybrid quantum circuits.

Of course, all this work is not a solo adventure. I would therefore like to thank all the talented researchers I've been working with during my young career, either during my PhD in the Quantronics Group (SPEC, CEA-Saclay), or my two successive post-docs in the Quantum Circuit Group (LPA, ENS) and in the Jarillo-Herrero Group (MIT). Now a permanent researcher at PMC, Ecole Polytechnique, I feel privileged to be able to develop and lead a new group with my childhood friend, and to work on a daily basis with my young and brilliant teammates from the QCMX Lab. I also want to acknowledge the friendly and healthy environment at PMC, the support from the staff at EP that was instrumental in some cases, the help from some colleagues at LSI, LLR, CPHT and PICM, and the great interaction with my brilliant fellows from the Physics Department. More generally, we are lucky to be part of a great community that is structured in France around the *Quantum Mesoscopic Physics GDR*. In particular, we benefit from the great help or our friends and colleagues at SPEC CEA-Saclay, LPENS, Collège de France, C12, ENS Lyon, UMPhy Thales, C2N, LPS and Néel Institute, as well as the support of some long-time foreign collaborators notably in the USA. Finally, I have a special thought for my dear friend Fabien Portier who left too early.

The QCMX Lab on Nov 24, 2021. The team celebrating the installation of their new dilution refrigerator at *La Belle Epoque*, Chateaufort (78)**.** From left to right: Ambroise Peugeot, Landry Bretheau, Samy Annabi, Jean-Damien Pillet, Joël Griesmar and Hannes Riechert. Not on the picture: Everton Arrighi has since then joined the QCMX Lab as a research engineer.

2 Andreev Bound States in single-atom contacts

I discovered the field of mesoscopic superconductivity during my PhD in the Quantronics Group (CEA-Saclay), under the mentoring of my advisors Hugues Pothier and Cristian Urbina. The most striking phenomenon in this field is the Josephson effect, which describes the coherent coupling between two superconductors and the resulting supercurrent. It has been extensively probed since its prediction in 1962 [1] and is the basis of many electronic devices with applications ranging from medicine to astronomy. Although all these devices are based on the same component, the superconducting tunnel junction, the Josephson effect can occur in any junction where two superconducting electrodes are coupled through a weak link, which can be a simple normal metal or a more exotic quantum conductor. In any case, the microscopic origin of the Josephson effect is that entangled electron-hole states form inside the weak link, and are responsible for carrying supercurrent. These fermionic states, called the Andreev bound states (ABS) [2–4], are analogous to Cooper pair states that are localized at the weak link, with a condensation energy E_A that depends on the superconducting phase difference φ across the weak link. They come in pairs and appear as discrete levels within the superconducting gap (see Fig. 1a).

Although ABS were predicted in the 60's, this fermionic degree of freedom was essentially ignored in experiments made with Josephson circuits prior to my thesis and the excited ABS had never been detected. To achieve this ambitious goal, I made several experiments, using a model Josephson weak link: a single-atom contact between two superconductors [5]. This system has just a few conduction channels whose transmission can be tuned *in-situ* using mechanical break-junctions. One can thus isolate just a few ABS. In the single channel case, the excitation spectrum is particularly simple [6–9] and consists of 2 Andreev levels (see Fig. 1a). The ABS correspond to the 4 possible configurations of this doublet (see Fig. 1b). The ground state $|-\rangle$ and the excited state $|+\rangle$ contain an even number of quasiparticles (0 or 2) and have zero spins. The odd states $|\uparrow\rangle$ and $|\downarrow\rangle$ contain one quasiparticle and have opposite and finite spins. Crucially, the energy of these states depends on the superconducting phase difference φ and each ABS carries a different supercurrent, which makes it possible to differentiate it from the others.

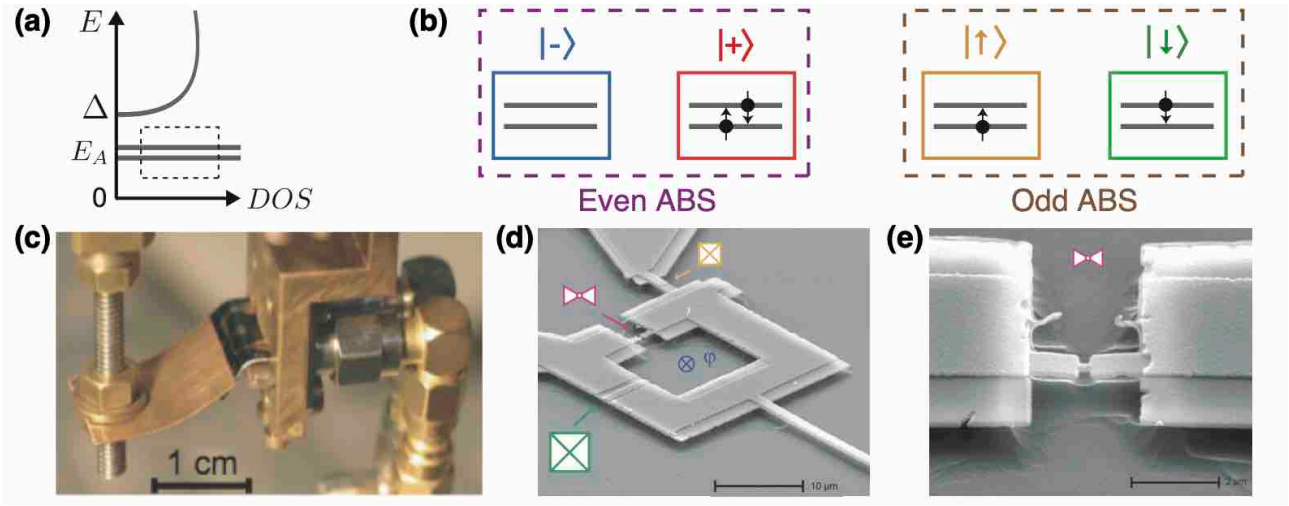

Fig. 1: Andreev Bound States in single-atom contacts. (a) Density of states within the weak link in the excitation representation: 2 non-degenerate Andreev levels lie inside the superconducting gap $[0, \Delta]$. **(b)** The ABS correspond to the 4 possible configurations of these 2 levels. **(c)** Experimental setup showing the bending mechanism and the Kapton sample: this break-junction technique makes it possible to get single-atom contacts. **(d,e)** SEM micrograph of the sample used in the ABS spectroscopy experiment discussed in Sections 2.2 and 2.3 showing the Josephson spectrometer (yellow), the atomic contact (magenta) and the SQUID Josephson junction (green).

2.1 Quasiparticle trapping in Andreev bound states

This section discusses results published in Refs. [10,11].

We have performed quantum transport experiments using atomic contacts made out of aluminum to measure the supercurrent carried by the ABS. In practice, the atomic contact was enclosed on a superconducting loop containing a large Josephson tunnel junction, thus forming an asymmetric SQUID. It is then possible to both extract the transmission coefficients of the contact and measure its current-phase relation. This technique had been previously used in the group to measure accurately the supercurrent as a function of phase in the ground ABS [12]. With Maciej Zgirski, post-doctoral associate in the group at the time, we designed and fabricated new samples with the goal of detecting the excited ABS. But for these new samples, we observed discrepancies from the expected behavior. For highly transmitting contacts the supercurrent was strongly reduced within a broad phase interval around π (see Fig. 2a). This reduction corresponds to the exact suppression of the Andreev supercurrent of the most transmitted channel [10,11].

We have shown that this effect is due to the trapping of spurious quasiparticles from the delocalized continuum states into the localized ABS (see sketch in Fig. 2c). This trapping therefore corresponds to an excitation from the even ground state $|-\rangle$, to either one of the odd excited states $|\uparrow\rangle$ or $|\downarrow\rangle$, which carry no supercurrent. The weak link thus behaves as a "superconducting quantum dot" that can trap quasiparticles. This trapping phenomenon is stochastic and leads to finite lifetimes for the odd states, which we measured as large as 200 μs (see Fig. 2b). This work evidenced the odd ABS and has shown that these excited states can have long life times. It is therefore very promising to explore their quantum properties and to control their spin. On the other hand, this discovery of quasiparticle poisoning in ABS has great consequences on the search for Majorana fermions as their existence and topological protection rely on parity conservation, which is broken due to quasiparticle poisoning.

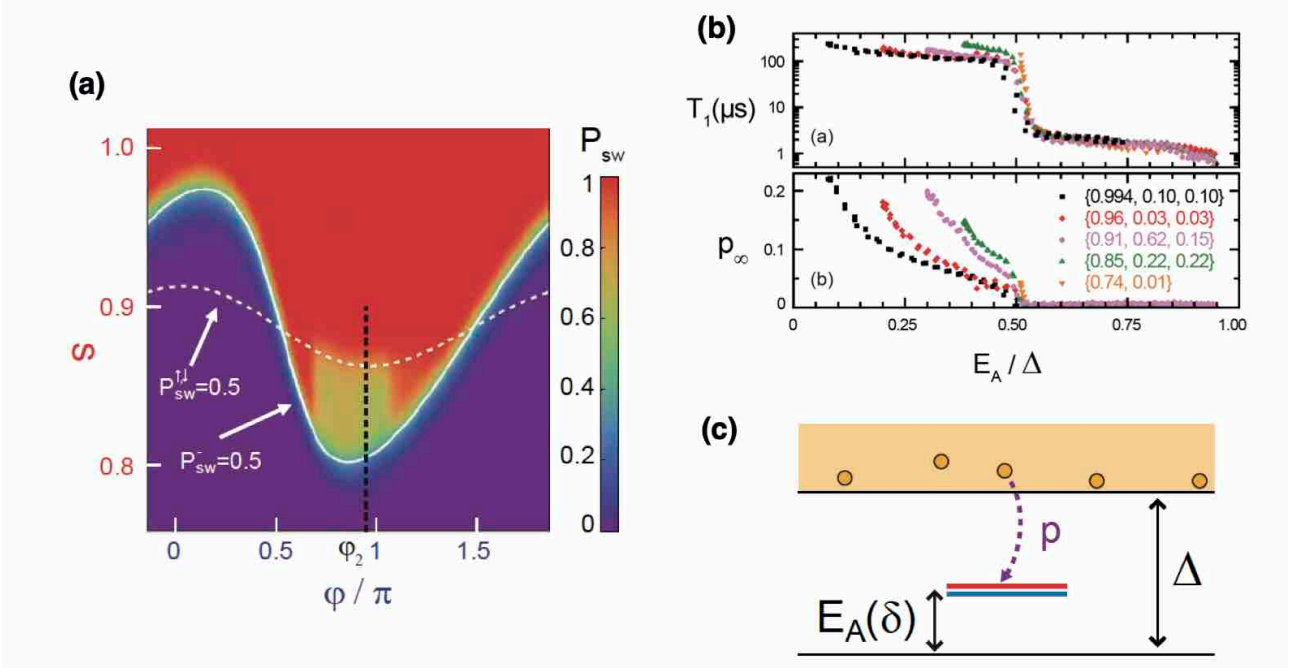

Fig. 2: Quasiparticle trapping in Andreev bound states. (a) Switching probability as a function of bias current and superconducting phase difference. It shows the stochastic suppression of the Andreev supercurrent carried by the most transmitted channel in a broad phase region around π. **(b)** Measured lifetime and asymptotic probability of the odd ABS as a function of the Andreev energy of the most transmitted channel. **(c)** Schematics for the trapping mechanism of quasiparticles in the ABS localized at the weak link with probability p.

2.2 Photon absorption spectroscopy of Andreev bound states

This section discusses results published in Refs. [13,14].

To detect the even excited ABS $|+\rangle$, we designed a new experiment together with Caglar Girit, post-doctoral associate in the group. The idea was to perform the photon absorption spectroscopy of the ABS. To do so, we used an additional Josephson tunnel junction as an on-chip broadband microwave spectrometer [15–22]. When biased at voltage V, this Josephson junction is crossed by an ac Cooper pair current that oscillates at the Josephson frequency $\nu = 2eV/h$ (see Fig. 3a). Therefore, it acts as an on-chip ac current generator. This ac current flows through the environment of the junction where it can excite electromagnetic modes. If this happens, a finite dc current flows through the junction to satisfy energy conservation, which corresponds to the inelastic tunneling of Cooper pairs through the insulating barrier that emit photons at energy $h\nu = 2eV$ (see Fig. 3b). Therefore, one can detect these electromagnetic modes by measuring the $I(V)$ characteristic of the junction, which behaves as on-chip broadband microwave spectrometer.

By capacitively coupling our Josephson spectrometer to the atomic SQUID, we were able to perform the photon absorption spectroscopy of the ABS [13]. In the measured spectrum, we clearly resolve the Andreev transition at energy $2E_A(\varphi)$ that strongly depends on the superconducting phase difference (see Fig. 3c). We also identify the plasma mode of the SQUID and its first harmonic, which hardly vary with phase and hybridize with the Andreev transition. We were able to quantitatively explain all of the observed transitions using a quantum model that takes into account both the Josephson spectrometer and the atomic SQUID [14]. This model incorporates the Hamiltonian of the ABS with no fit parameter using the independently measured transmission coefficients, which shows the generic nature of these results. This work realizes the first photonic spectroscopy of the ABS and therefore demonstrates the existence of the excited even ABS $|+\rangle$.

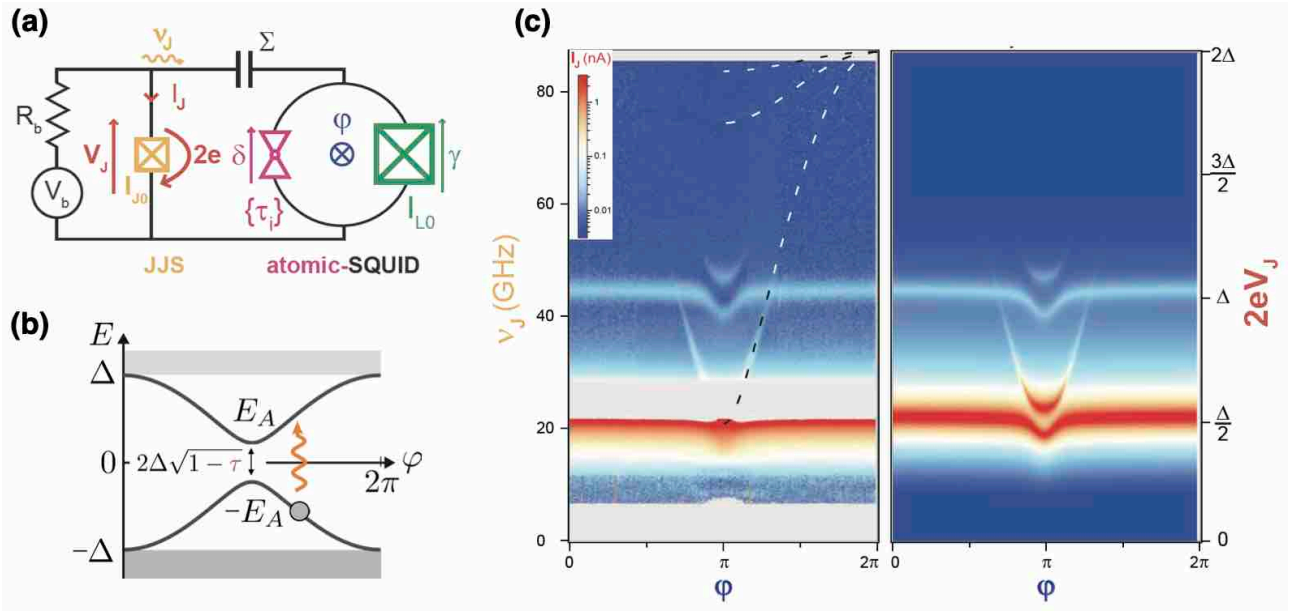

Fig. 3: Photon absorption spectroscopy of Andreev bound states. (a) Schematic of the setup: a voltage-biased Josephson junction, which behaves as a spectrometer, is capacitively coupled to an atomic-SQUIID. **(b)** Energy spectra of the even ABS as a function phase-difference: at resonance, the excitation can drive the Andreev transition. **(c)** Experimental **(left)** and calculated **(right)** spectra resolving both the Andreev transitions (dotted lines) and the plasma mode.

2.3 Supercurrent spectroscopy of Andreev bound states and beyond

This section discusses results published in Refs. [23,24].

Going further, we performed another experiment with the same system that showed the direct relationship between ABS and the Josephson effect. To do that, we still used an on-chip Josephson microwave emitter but with a different detection technique based on supercurrent switching measurements. The supercurrent is indeed proportional to the phase-derivative of the Andreev energy and therefore depends on the Andreev doublet occupation (see Fig. 4a). By measuring the change of supercurrent flowing though the atomic contact induced by the microwave irradiation [23], we could detect very sharp resonances associated with Andreev transitions from $|-\rangle$ to $|+\rangle$ at energy $2E_A(\varphi)$ (see red lines in Fig. 4b,c). We could also identify other transitions corresponding to excitation from the localized ABS to the continuum of states above the superconducting gap, at energies $\Delta + E_A(\varphi)$, that leaves the Andreev doublet in an odd configuration (blue lines in Fig. 4b,c). This work, which shows an improved resolution, directly demonstrates that the ABS indeed carry the supercurrent and are the microscopic building blocks of the Josephson effect.

Despite being obtained on a specific system, the superconducting atomic contact, these results are generic. They reveal the existence of an internal quantum degree of freedom to the Josephson effect that had been overlooked experimentally until then in the field of superconducting electronics. It was then natural to try to manipulate with light this exotic Andreev qubit, that could be a promising resource for quantum information. To investigate that, I designed a new experiment at the end of my PhD that coupled atomic contacts to narrowband microwave cavity in circuit QED architectures (see next section). I obtained promising preliminary results [25] that later culminated in the coherent manipulation of Andreev bound states by Camille Janvier and coauthors [24].

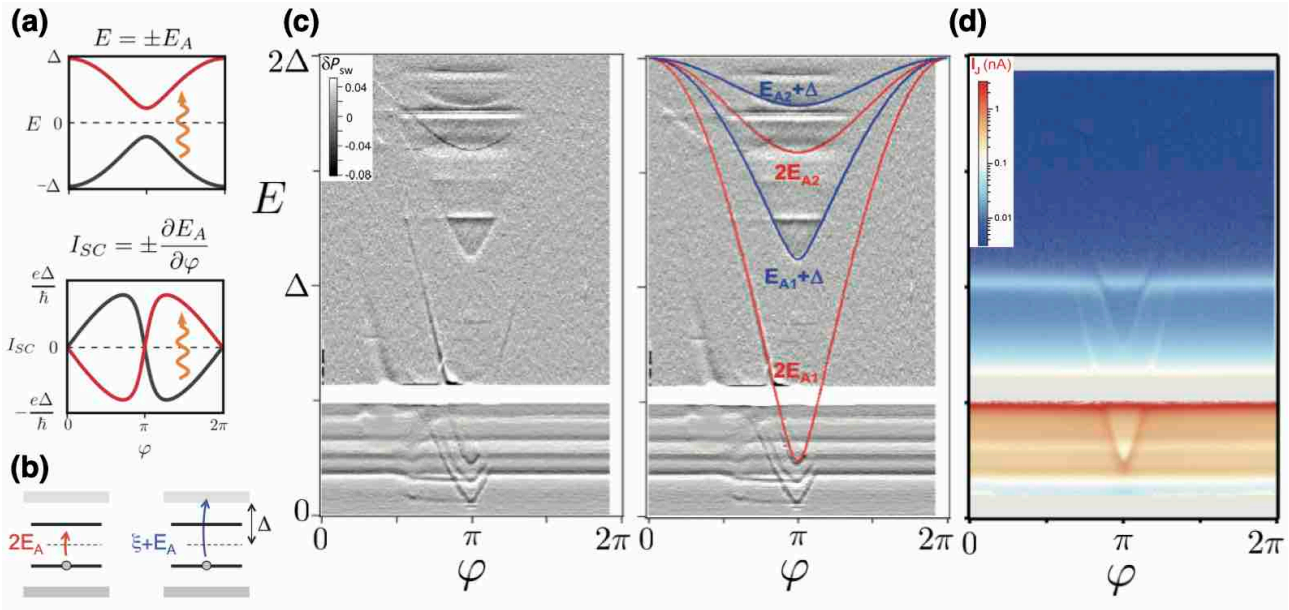

Fig. 4: Supercurrent spectroscopy of Andreev bound states. (a) Energy spectra and supercurrent of the even ABS as a function phase-difference: at resonance, the excitation can drive the Andreev transition and change the supercurrent. **(b)** Sketch of the different Andreev transitions. **(c)** Experimental (left) and calculated (right) spectra resolving both the Andreev transitions between even states (red lines) and the transitions to the continuum (blue lines). **(d)** Comparison with the absorption spectrum obtained for the same atomic contact.

3 Measurement back-action with quantum circuits

In 2013, I obtained a DGA post-doctoral fellowship and I joined the Quantum Electronics Group (ENS), led by Benjamin Huard. There, I discovered and explored the thriving field of circuit Quantum ElectroDynamics (cQED) [26], which was born in 2004 with the seminal work of Wallraff and coauthors [27]. It finds its roots in the 2012-Nobel-price-winning field of "cavity quantum electrodynamics" [28,29], which aims at studying the coherent interaction between light and matter at the level of the single atom and photon. In cQED, in place of atoms, Josephson tunnel junctions are used as two-level systems or quantum bits. These so-called "superconducting qubits" [30] can be strongly coupled to microwave photons, which are trapped inside superconducting resonators cooled-down at 10 mK. Using these elementary quantum systems, one can test the basic rules of quantum physics. This growing field of research has generated a huge number of experimental discoveries [26,31].

When I joined the young QElec Group, it had just achieved its first milestones experiments: the realization of a novel quantum limited amplifier, the Josephson mixer [32,33], and the demonstration of persistent control of a qubit by measurement feedback [34]. Together with Philippe Campagne-Ibarcq, PhD student in the group, I made several experiments to test the influence of measurement on elementary quantum systems. Quantum measurement is indeed known to disturb the state of a system. Is that possible then to track and manipulate the trajectory of a quantum system during a continuous measurement? In particular, how does each measurement result $m(t)$ affect the quantum state $\rho(t)$ over time (see Fig. 5a)? To answer these questions, we probed microwave electromagnetic modes that reside in superconducting circuits, in the so-called 3D transmon architecture [35,36]. A Josephson junction, which acts as a qubit, is enclosed in and coupled to a 3D cavity that behaves as a harmonic oscillator with equidistant energy levels (see Fig. 5b). We operate this bi-partite quantum system in the strong dispersive regime, which enables conditional qubit-photon logic, and can be described by the Hamiltonian:

$$H/h = f_q|e\rangle\langle e| + f_c a^\dagger a - \chi|e\rangle\langle e|a^\dagger a$$

with $a^\dagger$ & a the raising & lowering operators of the cavity, $|e\rangle$ the excited state of the qubit and χ the dispersive interaction frequency. All measurements were performed in the quantum regime $k_B T \ll hf$, using dedicated home-made quantum limited amplifiers.

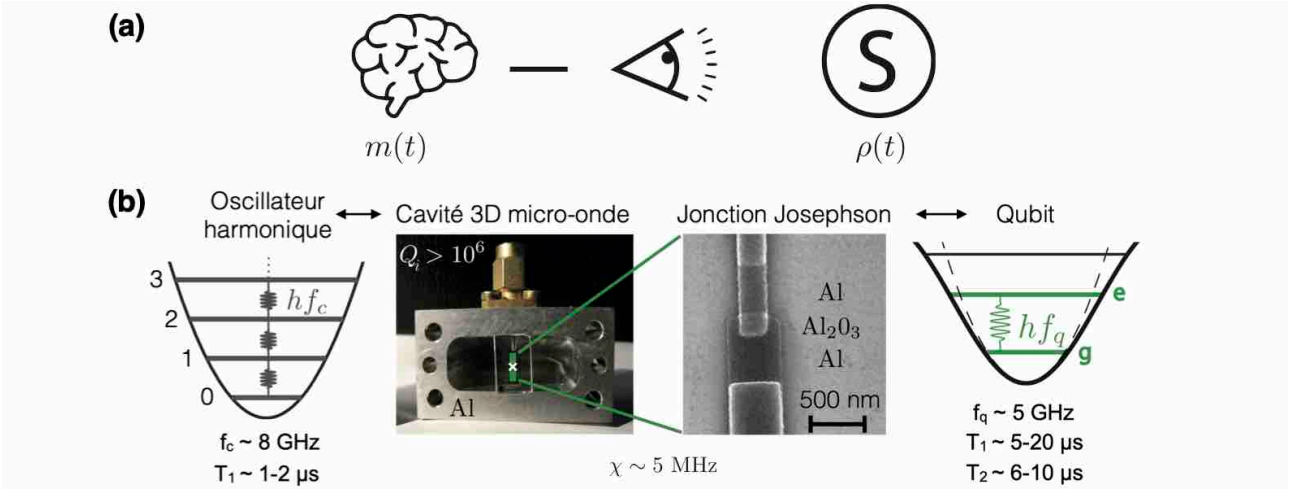

Fig. 5: Testing the influence of quantum measurement using a circuit QED architecture. (a) Schematic of a typical experiment: the observer measures an individual open quantum system prepared in state $\rho(t)$ and gets the measurement outcome $m(t)$. **(b)** Experimental setup: an Al/Al_2O_3/Al Josephson tunnel junction is fabricated on a sapphire substrate and behaves as a two-level system or qubit, with resonant frequency f_q. It is enclosed in and capacitively coupled to a 3D microwave cavity (made out of Al or Cu) that can be described as a harmonic oscillator, with frequency f_c. The typical values of the frequencies and coherence times are given in the figure.

3.1 Quantum measurement with past and future information

This section discusses results published in Ref. [37]*.*

Although quantum measurement is stochastic, its statistics can be predicted assuming some knowledge from the past. The state of an open quantum system, coupled to an environment and submitted to decoherence, can be described with a density matrix ρ. Starting from a known prepared state $\rho(0)$ at time 0, one can derive the system state $\rho(t)$ at any later time t using the Lindblad master equation and therefore predict the statistics of any measurement performed at time t:

$$\frac{d\rho}{dt} = -\frac{i}{h}[H,\rho] + \frac{\gamma}{2}(2\sigma_-\rho\sigma_+ - \sigma_+\sigma_-\rho - \rho\sigma_+\sigma_-)$$

Recently, a new formalism was developed to generalize quantum measurement theory by including information on the system's future [38–40]. One can indeed enforce what is the final state of the system by performing post-selection. The information about the future can be encoded in the effect matrix $E(t)$ that obey a similar master equation:

$$\frac{dE}{dt} = -\frac{i}{h}[H,E] - \frac{\gamma}{2}(2\sigma_+\rho\sigma_- - \sigma_+\sigma_-\rho - \rho\sigma_+\sigma_-)$$

Knowing the final state $E(T)$, one can derive $E(t)$ and thus *retrodict* the statistics of any measurement performed at time t. One can wonder then what happens when imposing both the initial state by preparation and the final state by post-selection (see Fig. 6a).

To test this new formalism, we have performed an experiment on the simplest open quantum system: a qubit in presence of a relaxation channel (see Fig. 6b). We have continuously measured, in the time domain, the fluorescence signal $s_-(t)$ emitted by the qubit at its resonant frequency [41], while it was driven at resonance and underwent Rabi oscillations. This implements a weak measurement of the qubit lowering operator $\sigma_- = |g\rangle\langle e|$, with a spread way beyond mean value where only partial information is extracted.

In a first set of experiments, we have prepared the qubit at time 0 in state $|e\rangle$. The average fluorescence signal is shown in Fig. 6c as a function of both time and Rabi frequency. One can recognize the usual damped Rabi oscillations of a qubit driven at resonance and submitted to decoherence, with a diminishing contrast of the oscillations and an increase of the qubit entropy. The measured average fluorescence is well modeled by

$$\overline{s_-(t)} = \mathrm{Re}\langle\sigma_-\rangle = \mathrm{Re}(\mathrm{Tr}[\sigma_-\rho(t)])$$

using the density matrix $\rho(t)$ that encodes information from the past.

To implement the time-symmetric version of the former experiment, we have prepared the qubit at time 0 in the maximally entropic state $(|g\rangle\langle g| + |e\rangle\langle e|)/2$ so that we have no knowledge of the system's past, we have let it evolve, and we have post-selected the qubit at time $T = 2.5\ \mu$s in state $|g\rangle$. The latter is performed by measuring in a single-shot manner σ_z at time T and selecting only the experiments that led to the outcome $|g\rangle$. The resulting average fluorescence signal is shown in Fig. 6d. It is indeed time-symmetric to the former experiment, with an increase of the contrast and a reduction of the qubit entropy for increasing time. The measured average fluorescence is well modeled by

$$\overline{s_-(t)} = \mathrm{Re}\big(\mathrm{Tr}\big[\sigma_- E(t)/\mathrm{Tr}[E(t)]\big]\big)$$

using the effect matrix $E(t)$ (whose trace is not 1) that encodes information from the future.

Finally, we have measured the average fluorescence signal for a qubit both prepared in state $|e\rangle$ and post-selected in state $|g\rangle$. This conditional average, which is shown in Fig. 6e, is dramatically changed with the appearance of negative (blue) and positive (red) pockets where the signal goes beyond the conventional range of unconditional averages, set by $|\mathrm{Re}\langle\sigma_-\rangle| \leq 1/2$. This violation is a purely quantum feature characteristic of the physics of weak values. It was predicted in the 80's in the famous paper by Aharonov and coauthors [42] entitled « how the result of the measurement of a component of a spin 1/2 can turn out to be 100 ». It was first seen in quantum optics by measuring the deflection of laser beams [43] and was more recently addressed with superconducting qubits [44,45]. This violation is a direct consequence of back-action in quantum physics. Two different measurements on a same system creates correlations which are larger than classically allowed. Actually, one can show that strong out-of-bound weak values occur when past and future information disagree. To model our experiment, we have used both the density and effect matrices:

$$\overline{s_-(t)} = \mathrm{Re}\langle\sigma_-\rangle_w = \mathrm{Re}(\mathrm{Tr}[\sigma_-\tilde{\rho}(t)]), \text{ where } \tilde{\rho} = \frac{\rho E}{\mathrm{Tr}[\rho E]}$$

This is in excellent agreement with the measurements (see Fig. 6f). Our experiment offers a quantitative test of this simple expression. More broadly, it allowed us to verify a recent formalism that put preparation and post-selection on the same footing and illustrates directly the back-action of measurement in quantum physics [37].

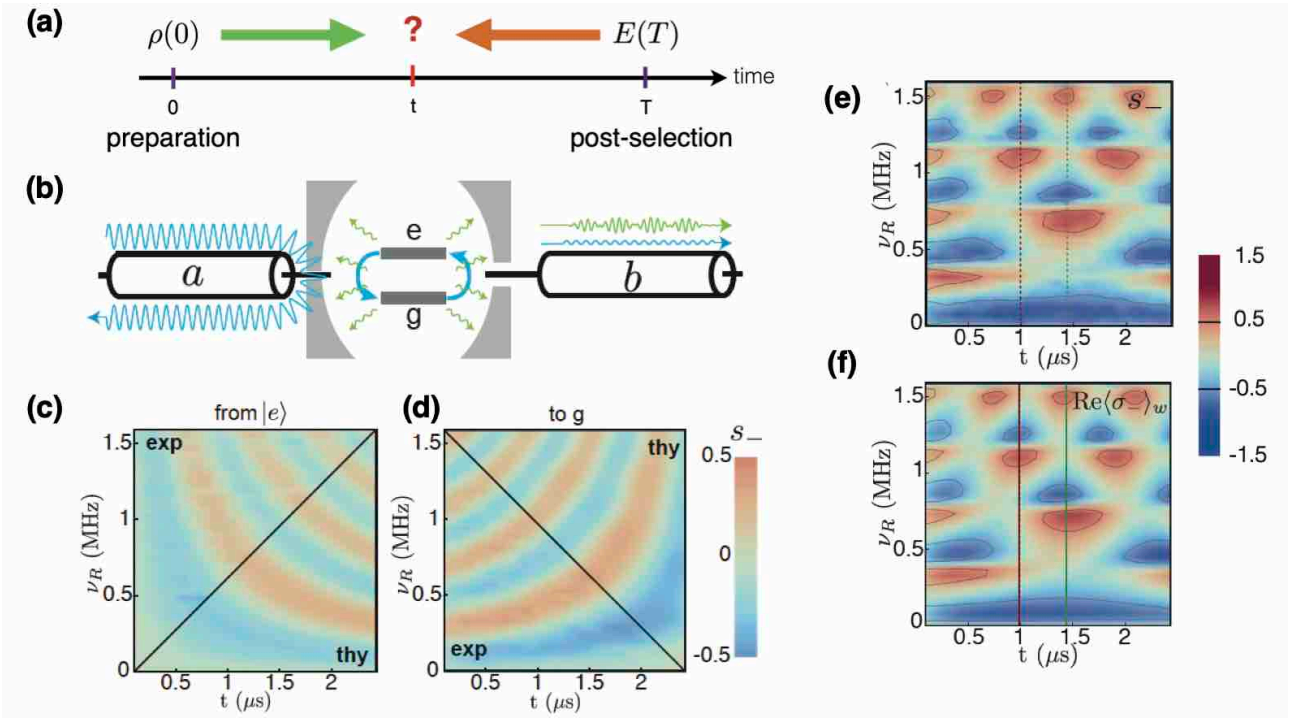

Fig. 6: Quantum measurement with past and future information. (a) Schematic of the experiment. **(b)** A qubit is enclosed in an out-of-resonance cavity. When driven at resonance with a resonant field via the weakly coupled line a (blue), the qubit undergoes Rabi oscillations while reemitting a fluorescence signal (green) on line b, which is further measured using a heterodyne detection setup that includes a quantum limited amplifier. **(c,d)** Average fluorescence signal as a function of both time and Rabi frequency, for a qubit either prepared in $|e\rangle$ (c) or post-selected in $|g\rangle$ (d). **(e,f)** Measured (d) and theoretical (e) average fluorescence signal as a function of both time and Rabi frequency, for a qubit prepared in $|e\rangle$ and post-selected in $|g\rangle$. Plain lines surround regions with weak values beyond the classical range $|\mathrm{Re}\langle\sigma_-\rangle| \leq 1/2$.

3.2 Diffusive quantum trajectories of a relaxing qubit

This section discusses results published in Refs. [46,47].

One can go further than measuring the mean fluorescence signal. From each individual measurement time trace, one can indeed extract the succession of quantum states occupied by the qubit in a single experiment, which is known as the quantum trajectory. To do this, one needs to use the stochastic master equation [48], which allows one to continuously update the state of a system $\rho(t)$ as a function of the outcome of a continuous measurement. Peculiar to quantum physics, quantum trajectories depend on the type of detection. In case of photocounting, the qubit would undergo discrete quantum jumps. In contrast, Wiseman and Milburn showed 30 years ago that heterodyne measurement of fluorescence should lead to continuous quantum state diffusion [49]. Experimentally, quantum jumps have been observed in a variety of physical systems [48], in particular recently in the field of cQED [50–52]. All these experiments were performed by detecting an ancillary microwave cavity to which the qubit was coupled and thus inferring the qubit population operator $\sigma_z = |e\rangle\langle e| - |g\rangle\langle g|$. Here instead, we have performed a direct heterodyne measurement of the light emitted during qubit decay, thus implementing a weak measurement of the qubit lowering operator $\sigma_- = |g\rangle\langle e|$, without any ancillary system in the original spirit of Ref. [49].

In practice, our fluorescence measurement is degraded by non-radiative decay processes of the qubit meaning that we do not collect all the photon emitted by the qubit. By designing a new experiment and using a dedicated phase-preserving quantum limited amplifier (see Fig. 7a), we reached a larger detection efficiency $\eta = 24\,\%$, which allowed us to detect individual quantum trajectories with relatively large purity. Without drive and starting from the initially prepared pure state $|e\rangle$, we let the qubit relax and measured the fluorescence field during 10 μs. The resulting record (dI_t, dQ_t) is then integrated over bins $dt = 200$ ns chosen so that $dt \ll T_1 = 4$ μs (see Fig. 7b). Using the appropriate stochastic master equation [46,53], one can extract from each individual measurement trace the corresponding quantum trajectory of the qubit, that is represented in the Bloch sphere in Fig. 7c. At each time step, only partial information is extracted from this weak measurement and the qubit state evolves erratically by "small steps" towards the ground state $|g\rangle$, in agreement with quantum state diffusion.

Going further, we could probe the statistics of these diffusive trajectories which are all different due to the stochastic nature of measurement. Fig. 7d shows the distribution of the qubit states at various times t for 10-µs-long trajectories, for a qubit starting either in $|e\rangle$ or $(|g\rangle + |e\rangle)/\sqrt{2}$. Starting from a single point, the state distribution progressively spreads out and collapses down to $|g\rangle$ at long times. Remarkably, at each time in the evolution, all quantum states almost belong to the same spheroid in the Bloch sphere, independently of the initial state. This is a non-trivial consequence of the fact that the qubit decoherence is largely dominated by the pure decay rate with negligible pure dephasing rate [46]. This work therefore realizes a fundamental textbook experiment imagined in the 90's that shows how the state of a qubit diffuses during its relaxation, at the single trajectory level.

In an immediate subsequent experiment [47], we have gone one step further by designing and implementing an analog feedback loop which consists of a control field whose value depends on the measured signal (see Fig. 7e). To do that, we have developed a multiple-input multiple-output analog Markovian feedback in the quantum regime. We have thus managed to stabilize any arbitrary state of the qubit at the level of each individual quantum trajectory (Fig. 7f). In practice, we could reach a maximum of 59% of excitation and 44% of coherence for the stabilized states thanks to our improved detection efficiency $\eta = 35\,\%$.

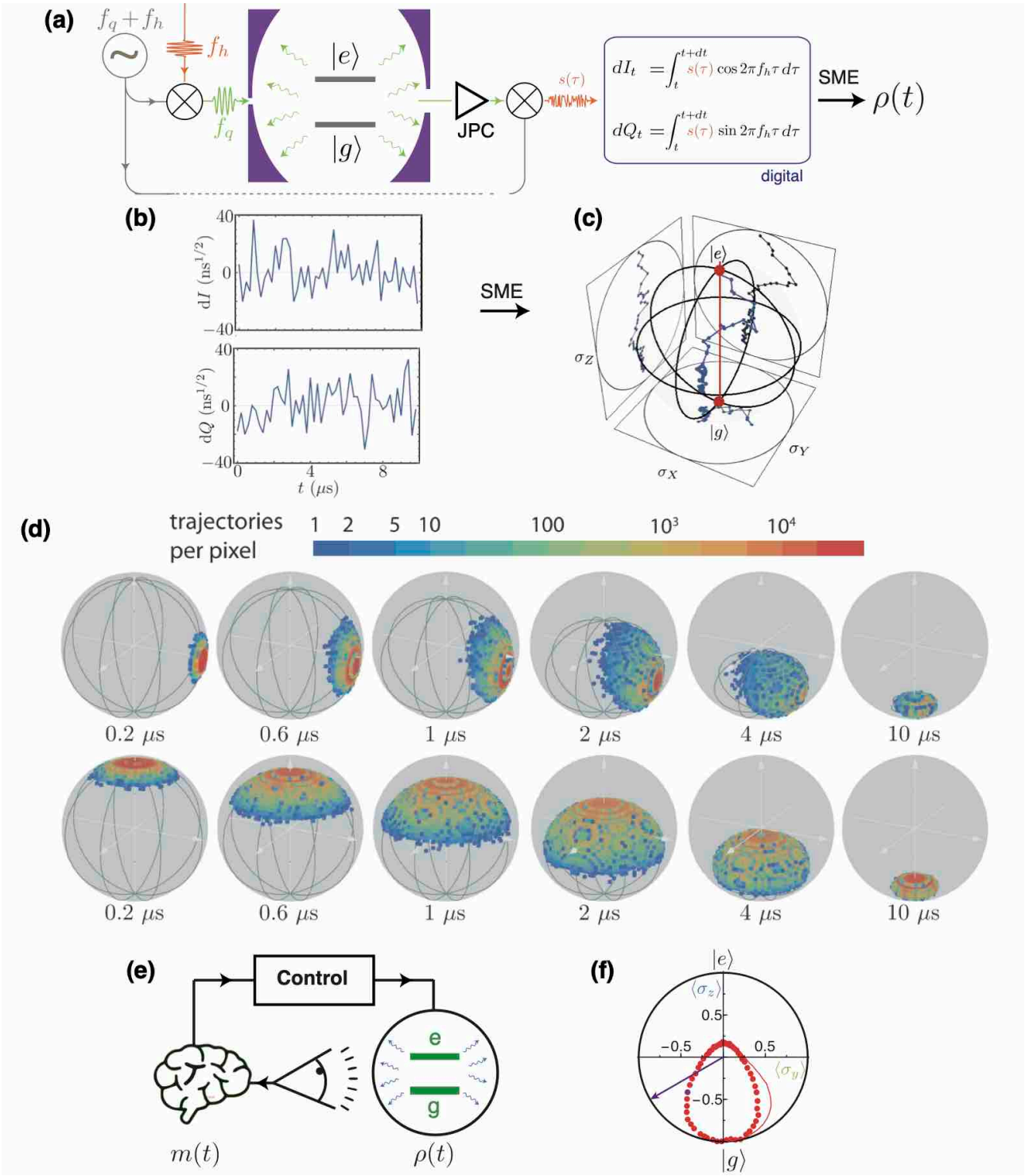

Fig. 7: Diffusive quantum trajectories of a relaxing qubit. (a) Schematic of the experiment. The fluorescence field of a superconducting qubit is recorded using a heterodyne detection setup that includes a quantum limited amplification (JPC), down-convertion and numerical demodulation into the quadratures (dI_t, dQ_t). The quantum trajectory $\rho(t)$ is then computed using the stochastic master equation. **(b)** Exemple of an individual measurement record of the fluorescence signal as a function of time, for a qubit initially prepared in $|e\rangle$. **(c)** Using the stochastic master equation, one can reconstruct the corresponding quantum trajectory. **(d)** Statistics of quantum trajectories. Distributions of the qubit states along 10-µs-long trajectories for a qubit initially in $(|g\rangle + |e\rangle)/\sqrt{2}$ (upper row) or $|e\rangle$ (lower row). The number of trajectories reaching each cubic cell of side 0.04 is encoded in color, out of a total of 3×10^6. **(e)** Schematic for the feedback-stabilization of a quantum state. One continuously measures the spontaneous emission of a qubit and apply a control field whose value depends linearly on the measured signal. **(f)** Measured stabilized states (red dots) are shown in the Bloch sphere projected on the yz plane.

3.3 Quantum Maxwell demon

This section discusses results published in Refs. [54].

The initial goal of all of the former experiments was to developed an unusual expertise in the field of cQED, that is the capability of measuring the fluorescence signal of a relaxing qubit, at its resonant frequency. Our goal was to perform a different experiment belonging to the emerging field of Quantum Thermodynamics: implement a quantum version of the famous Maxwell demon thought experiment. During my post-doc, I designed this experiment together with Benjamin Huard, did some preliminary work, and it was subsequently implemented and performed in the group [54]. I here give a brief description of it.

In this experiment, a microwave cavity plays the role of the demon and a qubit the one of a thermalized system, or bath, from which work is extracted (see Fig. 8a). The idea is the following. Starting from a qubit in the maximally "hot" state $(|g\rangle\langle g| + |e\rangle\langle e|)/2$ and a cavity in the vacuum state $|0\rangle$, we apply a displacement pulse to the cavity at frequency f_c conditional to the qubit being in state $|g\rangle$, thus creating the entangled state $(|g\rangle\langle g|\otimes|\alpha\rangle\langle\alpha| + |e\rangle\langle e|\otimes|0\rangle\langle 0|)/2$, such that the demon "knows" what is the system state. Then, by applying a π-pulse to the qubit at frequency f_q conditional to the cavity being in state $|0\rangle$, the qubit releases a photon due to stimulated emission when its state is $|e\rangle$ but does not absorb any photon when its state is $|g\rangle$. Therefore, the system ends up in the product state $|g\rangle\langle g|\otimes(|0\rangle\langle 0| + |\alpha\rangle\langle\alpha|)/2$, i.e. the entropy has been transferred from the qubit-bath to the cavity-demon.

We have implemented such an experiment and have measured the extracted work associated to this extra photon by detecting the fluorescence signal (see Fig. 8b), thus showing that one can indeed extract work from entropy. On top of that, by measuring the quantum state of both qubit and cavity, we could track the entropy flow and quantify the information remaining in the demon's memory (see Fig. 8c). To perform a complete thermodynamic cycle, one would need to erase the demon's memory, which could be done by connecting it to a 2nd bath and thus resolve the apparent paradox. The laws of thermodynamics are safe! This experiment illustrates the Maxwell's demon apparent paradox at the quantum level and demonstrates the intimate relationship that exists between information and thermodynamics.

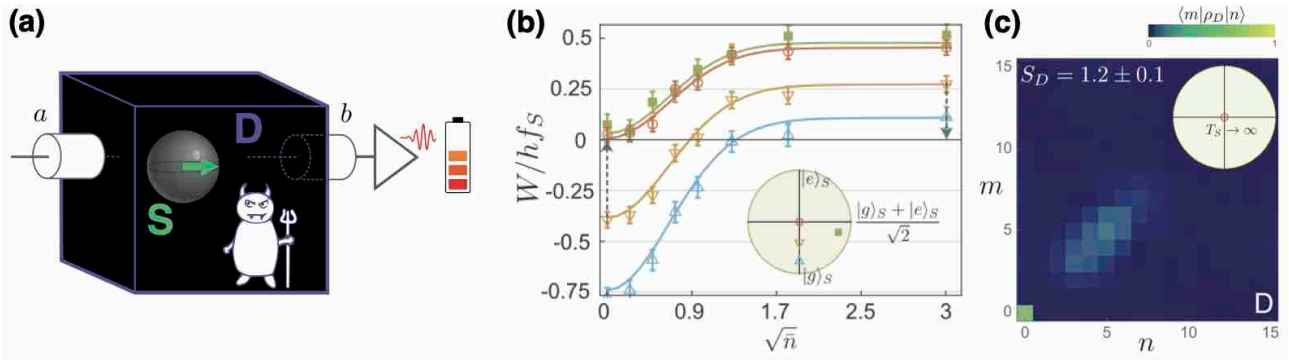

Fig. 8: Quantum Maxwell Demon. (a) Schematic of the experiment. A microwave cavity acts as a demon and is able to extract work from a hot qubit by knowing its quantum state. **(b)** Total extracted work as a function of $\sqrt{n}$, for different initial qubit state. The number of photons in the demon memory n quantifies the capability of the demon to discriminate between the states $|g\rangle$ and $|e\rangle$ of the qubit. **(c)** Tomography of the demon state at the end of the sequence for $\alpha = 0.25$. The corresponding von Neumann entropy is given in inset. The excess of entropy arises from imperfections of the experiment (dissipation and nonlinearity of the cavity).

3.4 Quantum Zeno dynamics of light

This section discusses results published in Ref. [55]*.*

By repeatedly measuring a system, one can freeze its dynamics owing to the back-action of strong projective measurements. This is the so-called quantum Zeno effect named after the Greek philosopher, which was first measured with trapped ions and more recently with superconducting qubits [44]. Interestingly, if the measurement projects the system not on orthogonal states but on multidimensional manifolds, evolution is possible inside of each stabilized subspace. Thus, the dynamics of the system is therefore dramatically modified but not frozen. The resulting constrained dynamics, restricted to a smaller Hilbert space, are then called Quantum Zeno Dynamics (QZD) [56–60]. Alternatively, a similar phenomenon can be achieved by using a strong, active coupling to an ancillary quantum system. Although no measurement is involved, such a dynamical decoupling effect belongs to the same class of dynamics in a restricted Hilbert space that is generally named QZD [58]. These ideas have recently been demonstrated for atoms, using either Rb Bose-Einstein condensates [61] or Rydberg atoms [62]. In this experiment, we have performed QZD of a single electromagnetic mode of light.

In practice, we have considered the resonant mode of a microwave cavity as our system of interest. This experiment was performed in a 3D transmon architecture, in the strong dispersive regime, still described by the Hamiltonian:

$$H/h = f_q|e\rangle\langle e| + f_c a^\dagger a - \chi|e\rangle\langle e|a^\dagger a$$

This enabled us to use the qubit as a photocounter since the qubit frequency depends on the cavity state. Indeed, a tone at frequency $f_q - N\chi$ addresses only the transition between states $|N\rangle\otimes|g\rangle$ and$|N\rangle\otimes|e\rangle$ as the dispersive shift $\chi = 4.63$ MHz is much larger than the level width that is dominated by the cavity decay rate $\gamma_c = (1.3\,\mu s)^{-1}$. Thus, under such a continuous drive, these levels hybridize and repel each other, with a splitting given by $\Omega_R = 6.24$ MHz that is proportional to the drive amplitude. Any transition to level $|N\rangle$ is now forbidden when the cavity is driven at resonance. Schematically, level $|N\rangle$ has been moved out of the harmonic ladder (Fig. 9a).

We have probed the cavity state as a function of time, while it was both submitted to a blocking tone at frequency $f_q - N\chi$ and driven at resonance f_c. First, we measured the Fock state probability $P_k = \langle k|\rho|k\rangle$ by sending a π-pulse at frequency $f_q - k\chi$ and detecting the probability to find the qubit in the excited state. Fig. 9b shows P_k as a function of time, for different values of N. After an initial increase similar to a coherent state, the level distribution bounced off a wall at $k = N$ and exhibits coherent oscillations. Since the electromagnetic mode is initially in the ground state, it cannot reach the blocked level $|N\rangle$ and remains confined to levels $|0\rangle$ to $|N-1\rangle$. The field dynamics is therefore dramatically changed and resembles that of an N-level system, or spin $(N-1)/2$. Our measurements are well modeled by considering the cavity Hamiltonian within a truncated Hilbert space and taking into account relaxation via a Lindblad master equation.

Going further, we have performed the direct Wigner tomography of the field as a function of time. The Wigner function is a complete representation of the quantum state of the field and can be expressed as $W(\alpha) = \mathrm{Tr}\left(D_\alpha P D_\alpha^\dagger \rho\right)$, where $D_\alpha = \exp(\alpha a^\dagger - \alpha^* a)$ is the field displacement operator and $P = \exp(i\pi a^\dagger a)$ is the photon parity operator. The latter is accessed using a method developed and applied in Refs. [63–65] where the qubit interacts with the cavity for a time $\tau = 1/(2\chi) = 108$ ns and is then measured. The measured Wigner functions for the field state are shown in Fig. 9c at various times during the first oscillation period for blocked levels $N = 3$ and $N = 4$. Starting from the vacuum state, the field is

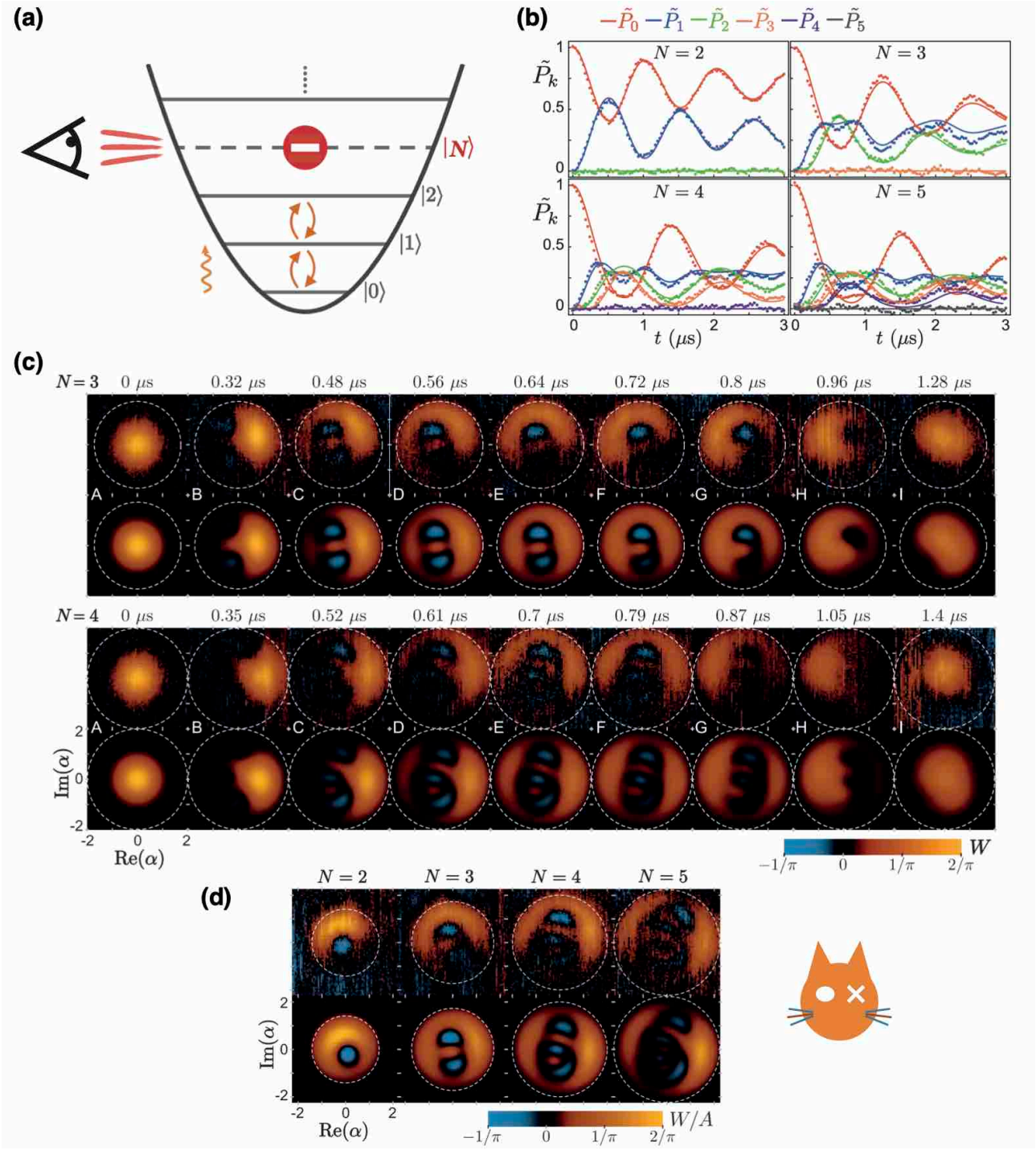

Fig. 9: Quantum Zeno dynamics of light. (a) Principle of the experiment: a continuous strong measurement prevents the access to the Fock state $|N\rangle$ of a microwave cavity that behaves as a harmonic oscillator. When driven at resonance, this oscillator is therefore confined to the first N levels and the field dynamics is dramatically changed. **(b)** Measured (dots) and theoretical (solid lines) photon number state probabilities as a function of time. The blocked level N ranges from 2 to 5 and is indicated on each panel. **(c)** Measured (top rows) and calculated (bottom rows) Wigner functions as a function of the displacement amplitude α, for a blockade at $N = 3$ (top panel) and $N = 4$ (bottom panel). The field is confined in phase space by a barrier at amplitude $\alpha = \sqrt{N}$ (white dashed circle). Negative values of the Wigner function, in blue, demonstrate the nonclassical nature of the field produced under QZD. **(d)** Measured (top row) and calculated (bottom row) Wigner functions of the cavity field for various blockade levels N from 2 to 5, taken at half period. The color scale is rescaled compared with (c) by $A = 0.7$. Analogously to Schrödinger cat states, these states exhibit fringes with alternating positive and negative values.

displaced due to the coherent drive until it hits a wall in phase space at $\alpha = \sqrt{N}$ and bounces back. After a full oscillation period, the cavity goes back to a state close to the vacuum state. Besides confirming the confined and periodic evolution of the field under QZD, this tomography reveals the formation of nonclassical field states, as indicated by the appearance of negative values in the Wigner function. They are most pronounced at half period, where the state is close to a Schrödinger cat state and exhibits fringes with alternating positive and negative values (see Fig. 9d). Once again, our modeling is in good agreement with the measurements. On top of its fundamental interest, this experiment demonstrates a new method of quantum control, tailoring the Hilbert space in time, and is potentially generalizable to many systems. It indeed allows to realize phase space tweezers for light, which can be used to prepare and control exotic quantum states of light, which are inaccessible otherwise.

4 Mesoscopic superconductivity in van der Waals materials

From 2015 to 2017, I worked as a Moore Fellow at the MIT, in the Jarillo-Herrero Group. There, I was immersed in a different research culture, more material science oriented, and I discovered the field of van der Waals materials. These two-dimensional layered materials can be "easily" isolated and mixed to form a wide range of heterostructures, which allows one to explore the intriguing physics that arise in 2D. They have been a central focus of materials research since the discovery of graphene in 2004 [66]. This single atomic layer of carbon atoms arranged in a hexagonal lattice possesses an exotic electronic band structure that hosts pseudo-relativistic quasiparticles [67]. This gives graphene remarkable physical properties [68], which were rewarded by the 2010 Nobel prize. Since then, graphene research was greatly boosted thanks to the introduction of hexagonal boron nitride (hBN) [69–71], an atomically flat, pristine, insulating, layered crystal that can be used both as a substrate, a gate dielectric, an encapsulating over-layer, and a tunneling barrier. On top of drastically improving the quality of graphene devices [72], hBN has opened up the new branch of low-dimensional van der Waals heterostructures [73].

When I joined the PJH group, it had just performed major experiments exploring the physics of magnetic focusing and quantum Hall effect in graphene [74–76]. All of these quantum transport experiments, that were performed at large magnetic fields (up to 9T) and moderately low temperature (up to 0.3 K), were probing relatively large energy scales that do not require few millikelvin temperature. My project, which I tackled together with Joel Wang, PhD student I supervised, was totally different and had more advanced requirements. Therefore, we had first to develop and install a new low-noise experimental setup compatible with quantum transport measurements at 20 mK, by equipping our cryostat with home-made electrical twisted-pair wiring and low-pass filters. This allowed us to probe the superconducting proximity effect in graphene.

4.1 Tunneling spectroscopy of Andreev bound states in graphene

This section discussed results published in Ref. [77]*.*

Graphene can exhibit low contact resistance and weak scattering when connected to superconducting electrodes [78,79]. These properties, combined with the ability to control the number of conduction channels with a gate voltage, make graphene an ideal test-bed for exploring Andreev physics in 2D. Although the superconducting proximity effect in graphene has attracted considerable research interest [80–88], most of the experimental studies have been limited to transport measurements of dissipationless supercurrent in graphene-based SGS Josephson junctions. Accessing the energy domain while controlling the superconducting phase difference is crucial for probing ABS. At the time, it had been performed in just a few systems, such as silver wires [89], carbon nanotubes [90,91], semiconductor nanowires [92], and atomic break-junctions [13,23]. However, a direct spectroscopic observation of phase-dependent ABS in graphene was missing.

To probe Andreev physics in the energy domain, we performed tunnelling spectroscopy of graphene proximitized by superconductors, using a full van der Waals heterostructure shown schematically in Fig. 10a. A monolayer graphene sheet is encapsulated between hexagonal boron nitride (hBN) crystals. The bottom one is 15nm thick and isolates graphene from a graphite local backgate, which enables us to control electrostatically the Fermi energy of graphene with the voltage V_g. The top hBN crystal is just one atom thick and is used as a tunnelling barrier. Immediately on top sits a 150-nm-wide metallic probe made of thin graphite, whose small work function mismatch limits the doping in the graphene. This heterostructure is made by successive exfoliations, in the manner of a Lego. The 2 μm-wide

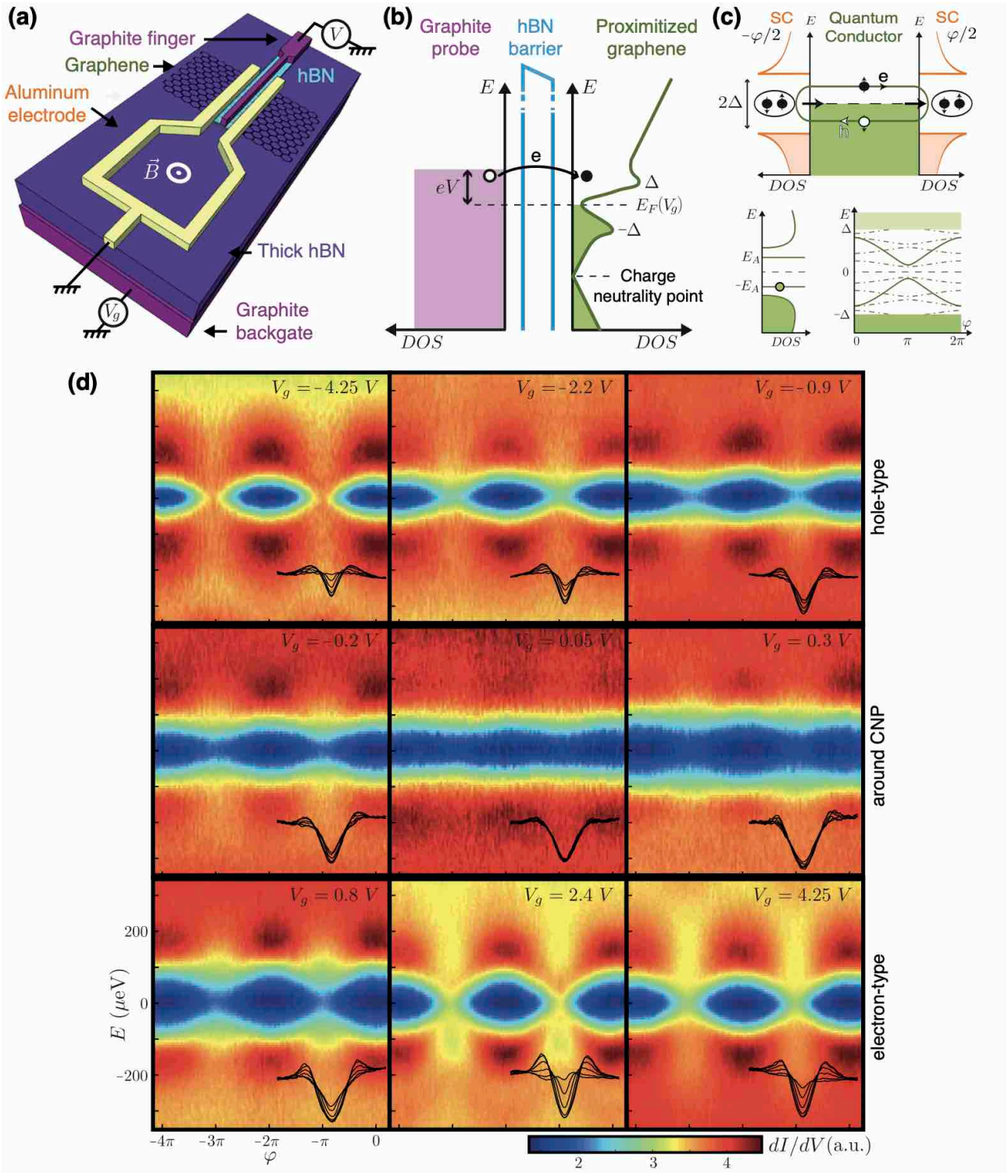

Fig. 10: Tunneling spectroscopy of ABS in graphene. (a) Device schematics. An encapsulated graphene flake is connected to two Al superconducting electrodes. Magnetic flux ϕ threading the loop imposes a phase $\varphi = \phi/\phi_0$ across graphene and modulates the Andreev states energy. **(b)** Schematics of the tunnelling spectroscopy process. The normal probe is a graphite electrode and the tunnelling barrier a monolayer hBN crystal. **(c)** Microscopic picture of the Josephson effect via the formation of phase-dependent ABS in the quantum conductor. **(d)** Normalized differential conductance measured as a function of both energy $E = eV$ and phase φ, for different gate voltages V_g (indicated in each panel). The solid black traces in each lower right corner correspond to cross-sections of the data at phases $\varphi/\pi = 0,\ 0.2, 0.4, 0.6, 0.8, 1$.

graphene sheet is well connected to two superconducting aluminum electrodes, with a 380 nm inter-lead distance. These electrodes are patterned in a loop that enables us to control the phase difference φ across the graphene by applying a magnetic flux through the loop.

By measuring the differential conductance of this tunnelling device at 20 mK, we could access the local density of states (DOS) in the graphene under proximity effect (see Fig. 10b). Fig. 10d shows tunnel spectra, as a function of energy and phase. The graphene DOS, usually featureless within this narrow energy range in the normal state, has dramatically changed due to the superconducting proximity effect. It displays a soft induced gap $\Delta \sim 160$ μeV, which oscillates with the superconducting phase difference. This demonstrates the presence of a continuum of ABS modulating with phase, which is expected for a spatially extended graphene. Since the SGS junction length is comparable with the superconducting coherence length $\xi \sim 0.6$ μm, the spectrum is complex and made out of different type of ABS. The phase-modulation is dominated by ABS associated with well-coupled channels in the short-junction regime (solid lines in Fig. 10c). At the same time, channels with large transverse momentum and / or low contact transparency provide ABS that fill the superconducting gap and exhibit weaker phase modulation (dashed lines in Fig. 10c), thus explaining the observed soft superconducting gap.

By changing the carrier density, a transition between different mesoscopic regimes is observed (see Fig. 10d). In particular, at low density close to the charge neutrality point (CNP), the phase modulation of the DOS is very weak, owing to the formation of electron–hole puddles due to disorder [72,93]. In contrast, at high carrier density, a complete closure of the gap is observed, demonstrating the presence of ballistic ABS. The effect of the normal scattering properties also appears as an asymmetry between the energy spectra for opposite carrier density. When the graphene is hole-doped, the phase modulation of the DOS is indeed smaller than in the electron-doped case. This is because aluminum n-dopes graphene underneath the contact due to their work function difference. This causes the formation of p–n junctions that reduce the contacts' transparency when $V_g < V_{CNP}$, thus repelling the ABS from the gap edges toward lower energy and weakening the phase modulation of the DOS, in good agreement with measurements of Al–G–Al Josephson junctions that show smaller supercurrent in the hole-doped region [80].

This experiment provided the first observation of ABS in superconducting Dirac materials and exhibited the direct connection between Andreev and Josephson physics. On top of that, we developed a new technique that can probe electronic density of states of any van der Waals material, providing access to new exotic phases of matter. Since this article was published, several works have applied this technique with great success [94–102].

4.2 Tunneling spectroscopy of graphene nanodevices coupled to large-gap superconductors

This section discussed results published in Ref. [95]*.*

We performed a follow-up experiment using a new device where graphene is coupled to niobium/niobium nitride (Nb/NbN) electrodes. Our initial motivation was to explore the interplay of superconductivity with the quantum Hall effect, which could lead to the detection of exotic quasiparticles. To do so, it is necessary to strongly couple low-disorder graphene to large critical field superconductors. Along this line, improvements in nanofabrication have led recently to the demonstration of high-field Josephson effect in ballistic graphene coupled to niobium, evidenced by Fabry-Perot oscillations of the supercurrent and anomalous Fraunhofer patterns [79]. Even more recently, it was shown that the Josephson effect could persist in the quantum Hall regime by coupling a graphene sheet to molybdenum-

rhenium [88]. To elucidate the origin of these phenomena, it is interesting to perform further studies such as phase-controlled tunneling spectroscopy.

Apart from the Nb/NbN electrodes, the newly fabricated device is quite similar to the one presented in the previous section, with some significant differences (see Fig. 11a-b). First, the graphene is fully encapsulated as a thick hBN layer was added on top of graphene and the graphite probe so that graphene is fully isolated from the organic residue that results from nanofabrication (in the previous experiment, there was just a single atomic layer of hBN on top of graphene). Second, the encapsulated graphene is connected at both ends to the Nb/NbN electrodes via 1-D edge contacts [103]. Third, the tunneling barrier is a bilayer hBN crystal in order to reduce the energy broadening associated with the tunnel probe. Finally, the full device actually consists of five superconducting loops built on the same monolayer graphene sheet. In each loop, the lead-to-lead distance for the graphene weak link is 440 nm, and the width ranges from 1.3 µm to 3.4 µm. Such a geometry allows for both spectroscopic and transport measurements in the same graphene flake. Indeed, by measuring the current between two neighboring loops, one can extract the Josephson critical current through graphene. Such a measurement is shown in Fig. 11c, as a function of the gate voltage. The Fabry-Perot oscillations in the critical current observed in the hole (or p-doped) region graphene junctions demonstrate that transport is ballistic in the graphene junctions. Typical tunneling spectra are shown in Fig. 11d. At zero phase, the DOS exhibits a hard induced gap (zero DOS at low energy), which demonstrates the strength of the proximity effect and the high transparency of the SG interfaces. The phase modulation is somehow similar to the one observed in the previous experiment, and reveals the presence of a continuum of ABS in graphene.

However, at some specific gate voltages we observed resonant out-of-gap energy features that depend on the phase difference (Fig. 11f,h). To understand their origin, we measured the differential conductance as a function of both energy and gate voltage, over a large energy range (Fig. 11e). On top of the induced gap at low energy, one can see Coulomb diamonds (addition energy of ~5–60 meV) associated with 5–20 nm size quantum dots (QD). Fig. 11g shows a zoom-in on a given diamond at low energy. The diamond boundary peaks that disperse in (eV, V_g) with a negative slope (hereafter called NSDP) split around zero energy and are accompanied by dI/dV peaks of opposite sign, while the positive slope diamond peaks (PSDP) are aligned. Similar effects were already observed in S-QD-S hybrid systems [104–108]. As schematized in Fig. 11i, the NSDP (respectively, PSDP) correspond to the alignment of the resonant dot level with the peak at the edge of the induced superconducting gap in the graphene DOS (resp. with the Fermi level of the graphite probe). The QD here behave as energy filters in the tunneling process from graphite to graphene. Out of resonance, the tunneling rate is weak and one directly probes the graphene DOS by measuring the differential conductance. At resonance, the latter is greatly increased and proportional to the derivative of the graphene DOS, which explains the observed positive-followed-by-negative dI/dV values. Further, when the phase difference is varied, the graphene DOS is modulated and the NSDP oscillate in energy. This phenomenon can therefore happen at positive or negative energy, depending on the gate voltage (Fig. 11f,h). To elucidate the origin of the observed nanometric quantum dots, which could be due to spurious defects [109] or be intrinsic [110], one could combine tunneling spectroscopy and nano-SQUID thermometry measurements.

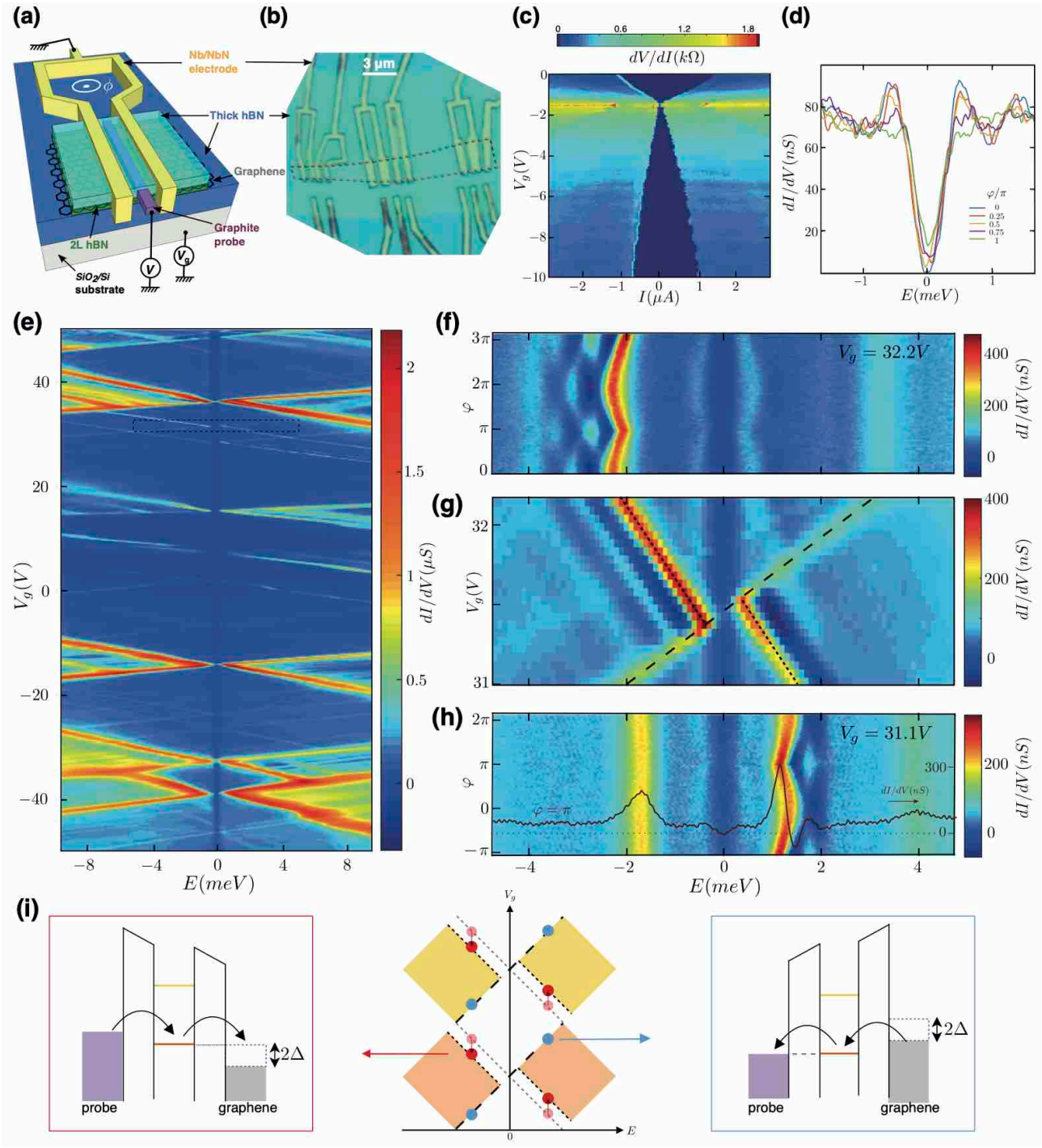

Fig. 11: Tunneling spectroscopy of graphene nanodevices coupled to large gap superconductors. (a-b) Device schematics and optical micrograph. A fully encapsulated graphene flake is connected to Nb/NbN superconducting electrodes. **(c)** Color-coded differential resistance of an S-G-S junction as a function of current bias and gate voltage. The critical current exhibits Fabry-Perot oscillations for hole doping. **(d)** DOS of proximitized graphene measured as a function of both energy and phase that exhibits a hard induced gap at zero phase. **(e)** Differential conductance as a function of both energy and gate voltage, at a large energy scale. **(g)** Zoom-in at the crossing of one Coulomb diamond, showing the splitting of the negative slope diamond peaks (NSDP) while the positive slope diamond peaks remain aligned across the induced gap. **(f,h)** Phase dependence of NSDP at two different gate voltages exhibiting a negative differential conductance associated with the derivative of graphene proximitized DOS. **(i)** Schematics of transport through a quantum dot connected to a normal and a superconducting electrode and resulting Coulomb diamonds with gap opening.

4.3 Electrically tunable low-density superconductivity in a monolayer tungsten ditelluride (WTe_2)

This section discussed results published in Ref. [111].

In parallel to the work presented before, I participated to an exciting project led by my MIT colleagues Sanfeng Wu and Valla Fatemi, both members of the PJH group (respectively Post-Doc and PhD student at the time). Their goal was to isolate and measure electrically a monolayer tungsten ditelluride (WTe_2), which belongs to the family of transition metal dichalcogenides (TMDs), materials that are either semiconductors or semimetals depending on their structural phase. In a first high-impact work, they had just demonstrated that monolayer WTe_2 behaves as a Topological Insulator and exhibits the Quantum Spin Hall Effect at temperatures up to 100 K, with the hallmark edge mode transport approaching the quantum of conductance $\sim e^2/h$ [112]. In a subsequent work, I helped them to characterize further monolayer WTe_2, by performing low-noise measurements in a dilution fridge at low temperature.

In practice, the device consists in a van der Waals heterostructure, with monolayer WTe_2 being encapsulated between hBN crystals, that are used both as a protection for this air-sensitive 2D material and as a low-dielectric constant material. The latter enables *in-situ* tuning of the charge carrier density by local field-effect gating. By measuring this material between 50 mK and 1 K, we have discovered that it can become superconducting. The critical temperature can be tuned electrostatically and is found to be as high as 950 mK. By decreasing the carrier density, we could continuously gate-tune the monolayer's ground state from the superconducting to the topological insulating state, and thus access the electronic phase diagram of monolayer WTe_2. At "zero temperature", the transition between these two very different macroscopic quantum ground states occurs at a critical doping density of $3 \times 10^{12}\ \mathrm{cm}^{-2}$. Such exceptionally low-density superconductivity is the key to this material extreme gate tunability. The observed unique phase diagram establishes monolayer WTe2 as a material for observing physics at the intersection of topological insulating states and superconductivity, and could allow to construct devices hosting Majorana zero modes to study non-Abelian physics.

5 Hybrid quantum circuits

In 2017, I was hired as an Assistant Professor at Ecole Polytechnique in tandem with my colleague and childhood friend Jean-Damien Pillet. We have been selected by an expert committee (including A. Aspect, A. Georges & D. Esteve), from a large pool of candidates, to a *position of excellence in Experimental Quantum Physics of Quantum Materials & Quantum Devices*. Since then, we have been building up from scratch a new laboratory dedicated to the experimental study of Quantum Circuits and Matter (QCMX Lab).

We are part of the Condensed Matter Physics Laboratory (PMC), which is a joint CNRS-Ecole Polytechnique research unit (UMR 7643) directed by Mathis Plapp. More specifically, we belong to the "Electrons, photons, surfaces" Team (EPS), directed by Jacques Peretti, which investigates the physics of localization in semiconductors, spin and exciton dynamics in semiconductors, and more recently of superconducting quantum circuits. In parallel with my research activity, I am a member of the Ecole Polytechnique Physics Department, directed by Silke Biermann, and I was appointed Professor in 2021. I teach quantum physics at the undergraduate level in the *Ingénieur Polytechnicien program*.

5.1 Building up the QCMX Lab

Prior to our arrival, experimental quantum physics in general, and the field of quantum circuits in particular, were not present at Ecole Polytechnique. To develop this new field of research, we have received laboratory space (~ 70 m^2), offices and a Young Team Fellowship (1.15 M€) from Ecole Polytechnique. On top of that, the team was awarded a DIM SIRTEQ grant from Region Ile de France (ONQC, 50 k€, 2018-2021), two individual ANR Young Researcher JCJC Grant from the French National Research Agency (QIPHSC, 320 k€, 2018-2023 / NEWS attributed to JDP, 335 k€, 2021-2025). More recently, I was awarded an ERC Starting Grant (FERMIcQED, 1.5 M€, 2021-2026) from the European Research Council Community.

Since we started literally from empty rooms, we first designed and planned the construction work of our two experimental rooms (electrical, masonry, plumbing), which were finalized in 2019. Using the above-mentioned grants, the laboratory has since been equipped with:

- a cryogen-free dilution refrigerator (T = 7 mK) with both DC and RF wiring (2019);
- microwave instruments (2019-2021): vectorial network analyzer, power spectrum analyzer, sources, cryogenic low-noise amplifiers, quantum orchestration platform;
- dc electronics instruments (2019-2021): high-accuracy voltage sources, current sources, low-noise amplifiers, lock-in amplifiers;
- a carbon nanotube fabrication platform (2020-2022): laser, spectrometer, camera, transfer station, microscope, furnace & gas handling system;
- accessories, tools, materials & electronic components (2018-2021);
- a cryogen-free dilution refrigerator (T = 10 mK), with a vector magnet (1T/1T/ 3T), fast-exchange loading mechanism (8h cool-down time) and DC / RF wiring (2021).

We have performed most of the setting up work of the lab and have recruited young group members. On top of the two PIs, the QCMX Lab is currently composed of Ambroise Peugeot (Post-Doctoral Associate since Oct 2020), Samy Annabi (PhD Student since May 2021), Hannes Riechert (PhD Student since Oct 2021), Joël Griesmar (Post-Doctoral Associate since Oct 2021) and Everton Arrighi (Research Engineer since Feb 2022). We are now working on our first experiments. For the nanofabrication (lithography, metal evaporation), we benefit from the shared cleanroom facilities of Paris and Saclay, in particular the cleanrooms located at Collège de France, SPEC-CEA and UMR CNRS-Thales.

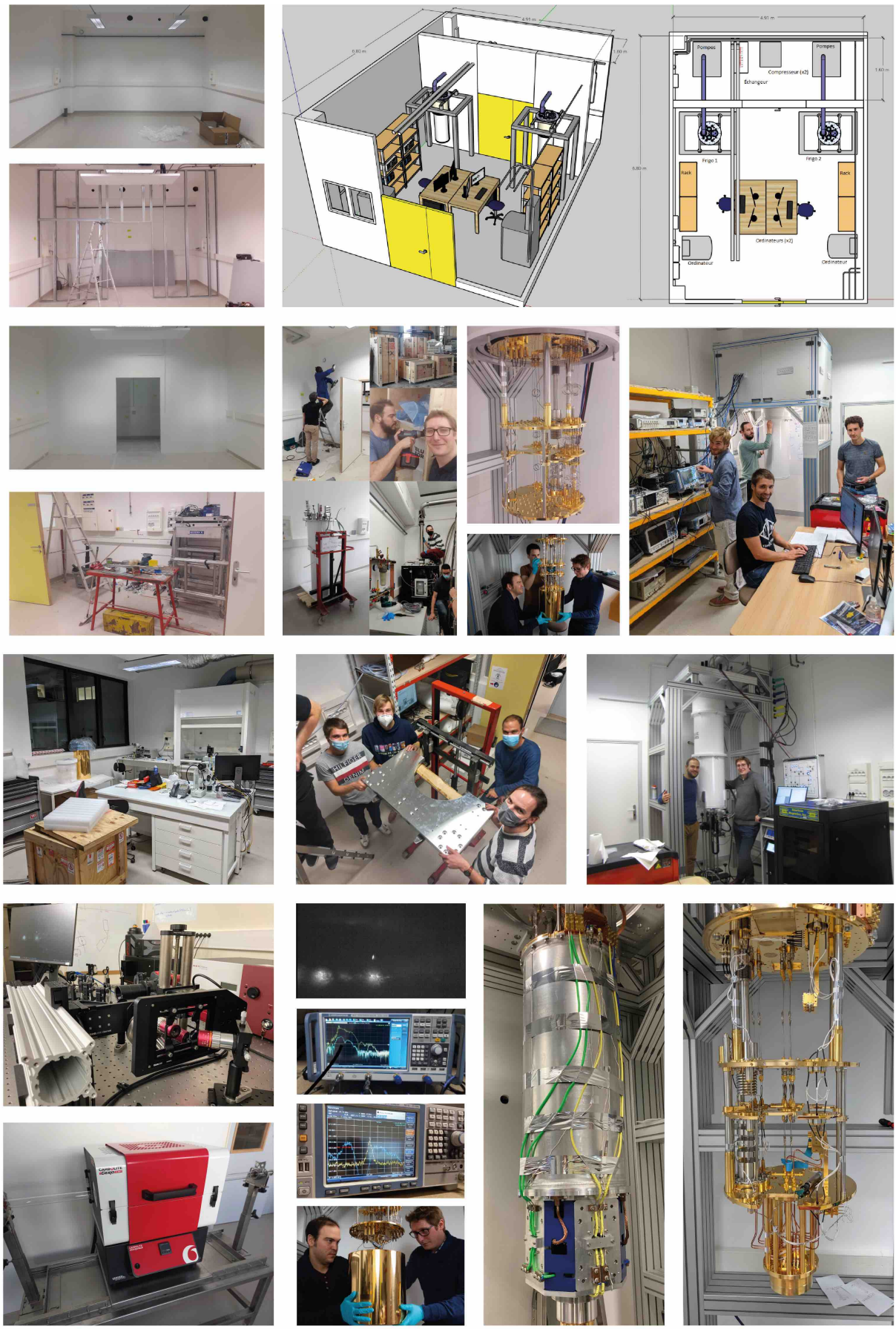

Fig. 12: Building up the QCMX Lab. Pictures and drawings of the lab featuring our measurement room (before and after construction works), preparation/nanofab room, dilution refrigerators, electronic instruments, optical platform and furnace for the carbon nanotubes.

5.2 Quantum coherence of a graphene-based superconducting qubit

This section discussed results published in Ref. [113].

While I was at MIT, I initiated a collaboration with the *Engineering Quantum Systems* Group led by Willliam D. Oliver. The EQuS group, which focus on the design, fabrication and control of superconducting qubits, was at the time of moderate size, and I had a close connection with them thanks to my background in cQED. After attending a talk by Charles Marcus on nanowire-based superconducting qubits, I proposed and designed a new project, at the interface between Will and Pablo's expertise. It consists in the realization of a novel hybrid superconducting architecture that implements a graphene-based superconducting qubit. Most superconducting qubits are based on tunnel Josephson junctions made out of aluminum. Instead of using an insulating barrier for the junction, we have used graphene as a weak link. This approach is directly inspired by the pioneering works from Copenhagen and Delft on so-called *gatemons* [114–118], nanowire-based transmons whose frequency can be tuned with a gate voltage capacitively coupled to the weak link. After an initial work of creation and design of the project while at MIT, I continued to work remotely from France on the project. My colleague Joel Wang was hired in the EQuS group as a postdoctoral associate to carry experimentally this project, with the help of Daniel Rodan-Legrain, PhD student from the PJH group that we co-supervised.

The experiment was performed using circuit Quantum electrodynamics architectures and techniques. The hybrid device consists of a $\lambda/2$ microwave resonator with bare frequency 7.34 GHz (Fig. 13b). It is capacitively coupled to a superconductor-graphene-superconductor (SGS) Josephson junction (Fig. 13a), where graphene is encapsulated within thick hBN crystals, transferred on top of an aluminum back-gate and contacted to lateral Al superconducting electrodes via 1D edge channels [103]. The Josephson junction is shunted by a large capacitance with charging energy $E_c/h = 100$ MHz, designed such that the qubit operates in the transmon regime $E_J \gg E_c$ where it is insensitive to charge noise [35,119–121]. To characterize the device, we first measured the microwave transmission through the resonator as a function of the readout frequency f_{ro}, around the bare-resonator frequency 7.34 GHz. The resonator spectrum is plotted in Fig. 13c as a function of the gate voltage V_g. We observe that the cavity resonance frequency f_R varies a lot with the gate, with a splitting at $V_g \approx -2.2$ V and -2.8 V. This demonstrates hybridization between the resonator and the qubit in the strong coupling regime.

Next, we performed a two-tone spectroscopy of the qubit by monitoring the qubit-state-dependent transmission through the resonator while varying the driving frequency f_{dr}. The corresponding qubit spectrum is plotted in Fig. 13d as a function of V_g and displays a qubit frequency f_{qb} that varies from 6 GHz to 12 GHz. The qubit spectrum reveals the characteristic electronic properties of the underlying graphene weak link. Indeed, the transmon qubit frequency is given by $hf_{qb} = \sqrt{8E_J E_C} - E_C$, with $E_J = \varphi_0 I_c$ the Josephson energy of the junction. We estimate a critical Josephson current of the SGS junction that varies with gate from ~ 90 nA to ~ 360 nA, consistent with our design and results reported in previous DC transport studies [80]. Varying the gate voltage changes graphene Fermi energy and electronic density of states, which translates into a change of the total number of transmission channels, of the Andreev spectrum [122] and of the corresponding Josephson energy of the SGS junction. Therefore, the measured 6 GHz-large tunability range of the qubit frequency is a direct consequence of graphene's peculiar electronic density of states (DOS), known as the Dirac cone, which is the one of a gapless semi-metal and which disperses linearly with energy. The qubit spectrum has a minimum at $V_g = V_{CNP} = -2.52$ V, where the Fermi level reaches the point with minimum density of states called the

charge neutrality point. The qubit spectrum shows clear asymmetry with respect to V_{CNP}, manifested as a lower f_{qb} value in the p-doped region with hole-like carriers ($V_g < V_{CNP}$), as compared to its equal-carrier-density counterpart in the n-doped region with electron-like carriers ($V_g > V_{CNP}$). This asymmetry arises from the n-type doping provided by the Ti/Al electrodes, which yields an n–p–n potential profile within graphene for $V_g < V_{CNP}$ (Fig. 13e) and results in two semi-transparent interfaces (p–n junctions) and therefore smaller I_c, E_J and f_{qb}. On top of that, this doping creates a Fabry–Pérot cavity for charge carrier with an effective length $L_C \sim 110$ nm inside the S–G–S junction, which results in constructive or destructive interferences when varying the Fermi wavevector $k_F \propto \sqrt{V_g}$, and which explains the f_{qb} oscillations observed in the hole-doped region. These Fabry-Pérot oscillations demonstrate that graphene is in the ballistic regime.

Going further, we have probed the qubit quantum coherence by performing operations in the time domain. Fig. 13f shows measurements of the qubit state while varying the drive frequency and the pulse duration for two different powers, measured at $V_g = -4.38$ V. At resonance, the qubit state undergoes Rabi oscillations between the ground state $|g\rangle$ and excited state $|e\rangle$, thus demonstrating that our system is indeed a qubit with finite quantum coherence. The Rabi oscillations are also used to calibrate the π-pulse (respectively $\pi/2$-pulse), which rotates the qubit state in the Bloch sphere about the x-axis by an angle π (resp. $\pi/2$). Thus, by applying a π-pulse that prepares the qubit in the excited state, we could measure after a variable delay an exponential decay trace with an energy relaxation time $T_1 \approx 36$ ns (Fig. 13g). Similar values were observed when varying the gate voltage and therefore qubit frequency, with T_1 ranging from 12 to 36 ns. To quantify further the graphene qubit coherence, we measured the dephasing for an equal qubit superposition $(|g\rangle + |e\rangle)/\sqrt{2}$. We have used Ramsey interferometry techniques, which consist in the application of two slightly detuned $\pi/2$-pulse separated by a varying delay time. Fig. 13 h-i show the corresponding Ramsey oscillations, which indicate coherent precession of the qubit state in the Bloch sphere around the z-axis. From the decay, we could extract a dephasing time $T_2^* \sim 55$ ns. This value being close to twice T_1 at the same gate voltage, our qubit coherence is currently limited by energy relaxation. Since the coherence times depend weakly on the gate voltage, they are probably dominated by the presence of other decay channels in parallel with the intrinsic loss of the graphene junction.

This work demonstrates the implementation of the first graphene-based superconducting qubit. These results suggest that van der Waals heterostructures are a promising alternative for extensible superconducting quantum computing. On top of that, these hybrid architectures could provide a new way to probe the dynamics of Condensed Matter systems.

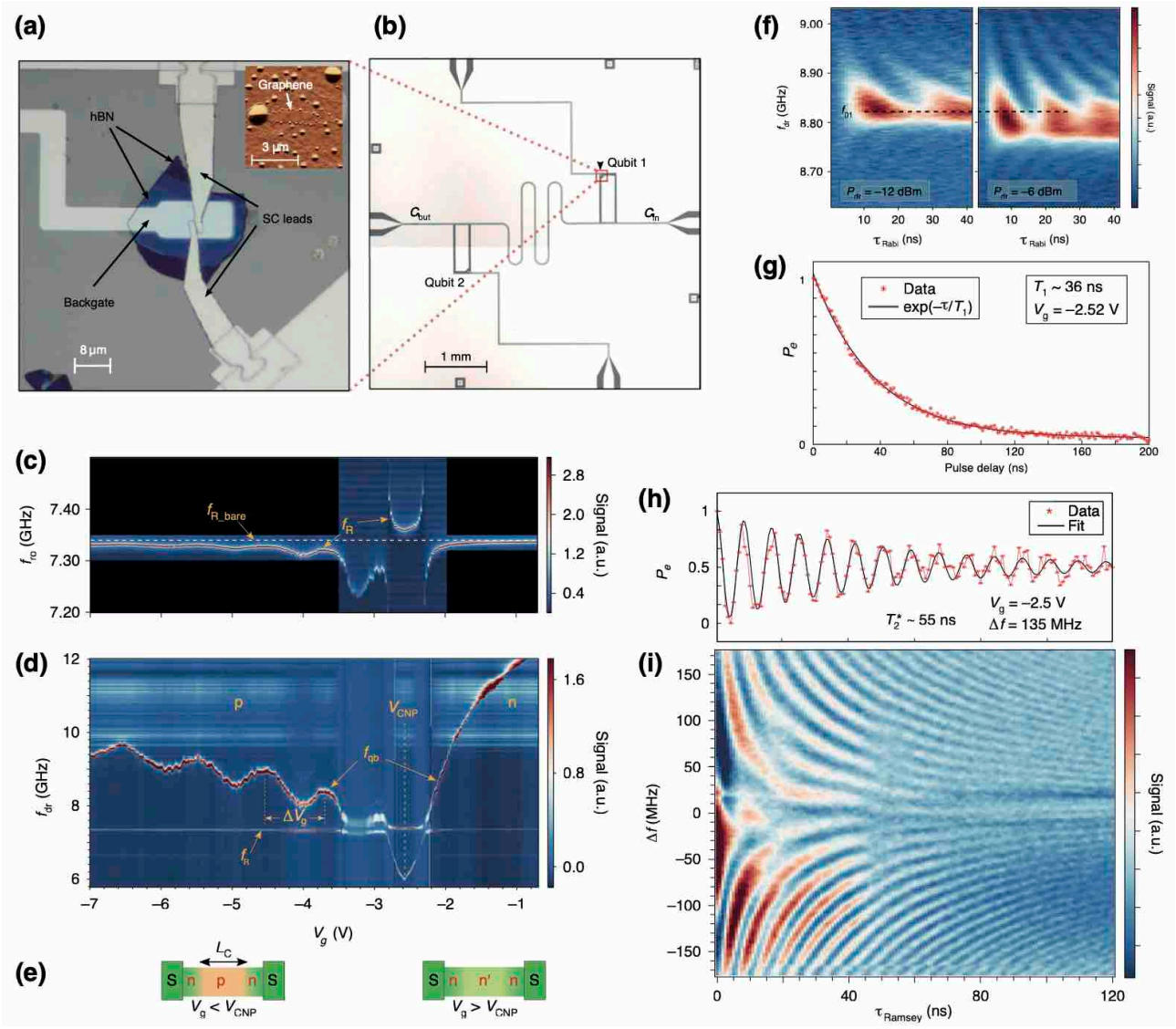

Fig. 13: Quantum coherence of a graphene-based superconducting qubit. (a) Optical micrograph of the graphene transmon qubit. Inset: AFM image of the encapsulated graphene before making electrical contact to the superconducting electrodes. **(b)** Optical micrograph of the whole chip. Two gate-tunable graphene transmon qubits are capacitively coupled to $\lambda/2$ microwave resonator. **(c)** Resonator spectrum as a function of readout frequency and gate voltage. The splitting demonstrates strong coupling and hybridization between the resonator and the qubit. **(d)** Qubit spectrum as a function of drive frequency and gate voltage, resulting from the gapless semi-metal linear DOS of graphene. Doping from the Ti/Al electrodes induced an asymmetry with respect to the charge neutrality point, with a reduced qubit frequency and the presence of Fabry-Pérot oscillations in the hole p-doped region. **(e)** Schematics of the graphene potential profiles in hole (p) and electron (n) regions. **(f)** Rabi oscillations of the qubit as a function of drive frequency and pulse duration, for two different drive powers, at $V_g = -4.38\,\mathrm{V}$. **(g)** Energy time relaxation T_1 after preparation in excited state $|e\rangle$, at $V_g = -2.52\,\mathrm{V}$. **(h-i)** Ramsey measurement of qubit dephasing in superposition state $(|g\rangle + |e\rangle)/\sqrt{2}$, at $V_g = -2.5\,\mathrm{V}$.

5.3 Topological Superconducting Circuits

This section discussed results published in Ref. [123].

During the 2020 Covid lock-down, I collaborated with Valla Fatemi (postdoctoral associate at Yale University) and Anton Akhmerov (PI at TU Delft) on a theoretical work related to topological superconducting circuits and Weyl physics. This story goes back to 1929, when Hermann Weyl envisioned the existence of new particles while reducing the relativistic Dirac equation to a two-component spinor equation in the case of massless particles [124]. These massless ultra-relativistic chiral fermions are called Weyl fermions. However, none of the elementary particles, observed or predicted in the Standard Model, are Weyl fermions. But they appear in Condensed Matter as quasiparticle excitations in so-called Weyl semimetals [125–128]. These are 3D materials with a band structure whose valence and conduction bands meet at discrete points with linear dispersion relation. These degenerate points, called Weyl nodes, come in pairs and are topologically protected, i.e. their existence is robust and does not depend on microscopic details or require special symmetries. The only way of removing such a Weyl node is to annihilate it with another node of opposite topological charge. Although predicted for a while, Weyl semimetals were discovered only very recently [129]. In these materials, the existence of Weyl nodes and their topological properties lead to physical consequences such as Fermi arcs surface states and the anomalous Hall effect. But experiments remain extremely challenging as it is difficult to disentangle topological effects from other standard effects in actual materials. That is why it is exciting to look for other systems to display Weyl physics, either by designing extended periodic structures such as photonic crystals or by performing simulations in the parameter space of a well-controlled system [130–136].

Along this line, we propose in this work to perform parametric simulation of Weyl band structures using superconducting quantum circuits made out of several tunnel Josephson junctions. We propose to harness the collective modes of these non-linear microwave-frequency circuits, that we baptize “Weyl Josephson circuits” (WJC). Four examples of such circuits are shown in Fig. 14a-c. They can all be described by a generic Hamiltonian which has a capacitive part and a Josephson part. On top of the number and phase operators of each node, this Hamiltonian depends on two types of classical parameters: the offset charges $\boldsymbol{n_g}$ that can be controlled with gate voltages and the reduced magnetic fluxes $\boldsymbol{\varphi_m}$ that can be controlled with magnetic fields. Since this Hamiltonian is periodic in $\boldsymbol{n_g}$ and $\boldsymbol{\varphi_m}$, one can map it onto a Bloch Hamiltonian, which is periodic in momentum $\boldsymbol{k}$. In practice, we can choose that some of the parameters play the role of effective crystal momenta $\boldsymbol{k}$, and the remaining are used as external control parameters $\boldsymbol{c}$:

$$H(\boldsymbol{n_g}, \boldsymbol{\varphi_m}) \rightarrow H(\boldsymbol{k}, \boldsymbol{c}) \rightarrow H(\boldsymbol{k})$$

Only the dependence in $\boldsymbol{k}$ then matters for the effective band structure, and $\boldsymbol{c}$ are used as additional external tuning parameters. For a given circuit and mapping choice, we conduct an analysis that allows us to determine which symmetries - either time-reversal or spatial-inversion symmetry - are conserved or broken. This symmetry analysis allows to formulate a general approach to design WJC of a desired dimensionality and symmetry class.

To be more specific, we now focus on the case of a WJC that is composed of 6 Josephson junctions (see Fig. 14a). With the mapping $\boldsymbol{k} = \boldsymbol{\varphi_m} = (\varphi_x, \varphi_y, \varphi_z) \in [0,2\pi]^3$ and the control parameters $\boldsymbol{c} = \boldsymbol{n_g} = (n_{g1}, n_{g2}, n_{g3}) \in [0,1]^3$, this WJC breaks spatial inversion symmetry while preserving time-reversal symmetry. For each value of $(\boldsymbol{\varphi_m}, \boldsymbol{n_g})$, one can diagonalize numerically the Hamiltonian and compute its eigen-spectrum. For simplicity and to present the generic physics, we consider first the case of symmetric junctions in the charge-

dominated regime $E_C \gg E_J$. Fig. 14d shows the energy spectrum as a function of the flux on the major diagonal of the Brillouin zone at charge degeneracy $\boldsymbol{n_{g0}} = \frac{1}{4}(1,1,1)$. We find degeneracy between ground and excited states at specific flux values, that we assimilate as Weyl nodes. Although these nodes' exact location in the Brillouin zone would change, their existence survives finite variation of the Hamiltonian parameters such as the Josephson and charging energies, non-uniformity, and the offset charges $\boldsymbol{n_g}$, thus demonstrating the topological protection. To illustrate that, we plot the gap E_g from the ground to the excited state while varying $\boldsymbol{n_g}$ away from $\boldsymbol{n_{g0}}$ (see Fig. 14e, from top to bottom). The central node first splits into 2 nodes, then the 4 nodes move, until they disappear with a fully gaped spectrum. To characterize the topological nature of these nodes, we compute the Berry curvature $\boldsymbol{\Omega}$, which is associated with derivatives of the eigen-function with respect to $\boldsymbol{k} = \boldsymbol{\varphi_m}$. It is plotted in black in Fig. 14f as a function of $\boldsymbol{\varphi_m}$, for different values of $\boldsymbol{n_g}$. We can see that the Berry curvature diverges at the nodes, as expected for Weyl nodes. By integration, we then compute the topological charge of each node $C(\boldsymbol{\varphi_m}) \in \mathbb{Z}$, which corresponds to an integer Chern number. The two external nodes have a charge $+1$ and the two central ones have a charge -1. When two Weyl nodes of opposite charge meet, they annihilate each other, signaling a topological phase transition (red dashed line). We go from a topological phase with four Weyl nodes, to a trivial phase with no Weyl node. This topological phase transition can be triggered *in situ* with the control parameter $\boldsymbol{n_g}$.

We can display the location of the Weyl nodes in the Brillouin zone (see Fig. 14g). To illustrate the robustness of this physics, this calculation is performed for non-uniform Josephson energies and asymmetric tuning of the offset charges. We still have 4 Weyl nodes as before, but they are now shifted off of the major flux diagonal. Remarkably and despite the circuit asymmetry, these Weyl nodes exist at opposite momenta with the same topological charge $C(\boldsymbol{\varphi_m}) = C(-\boldsymbol{\varphi_m})$. This is a direct consequence of time-reversal symmetry. Their existence and relation are topologically protected and do not depend on specific details of the circuit. This demonstrates that this circuit is a simulator of a minimal broken-inversion-symmetry Weyl semimetal with preserved time-reversal symmetry, as expected from the symmetry-based design. Going further, we design other types of Weyl Josephson circuits. We show that 3-junction circuits (see Fig. 14b) can implement minimal time-breaking inversion symmetric WJC, with two Weyl nodes located at opposite momenta with opposite charge $C(\boldsymbol{\varphi_m}) = -C(-\boldsymbol{\varphi_m})$. We can also design more complicated circuits that implement Weyl band structures of higher dimensionality (see Fig. 14c).

The topological properties of WJC could be probed experimentally using current nanofabrication and measurement techniques. The simplest experiment is microwave spectroscopy, using either cQED two-tone spectroscopy or Josephson spectroscopy [13,17,24,137]. The idea would be to observe Weyl nodes in the energy spectrum that annihilate following a topological phase transition. Another approach is to access the Chern number by performing low-frequency transconductance measurements [136]. By breaking open the circuit and applying 2 incommensurable dc voltages (see Fig. 14i), one can indeed sample a complete 2d plane within the Brillouin zone in flux (see Fig. 14g). This should lead to a dc current that is directly proportional to the Chern number (see Fig. 14h), and therefore to a quantized transconductance, which could potentially be useful for Metrology [138]. Finally, one could directly measure the Berry curvature as a function of the quasi-momenta, which is possible by going beyond adiabaticity [139]. This method is more involved as it relies on quantum coherence and was recently implemented with driven qubits to observe topological phase transitions [140,141]. These experiments provide observables that unavailable to topological materials, such as the in-situ triggering of topological phase transitions or the measurement of Berry curvature.

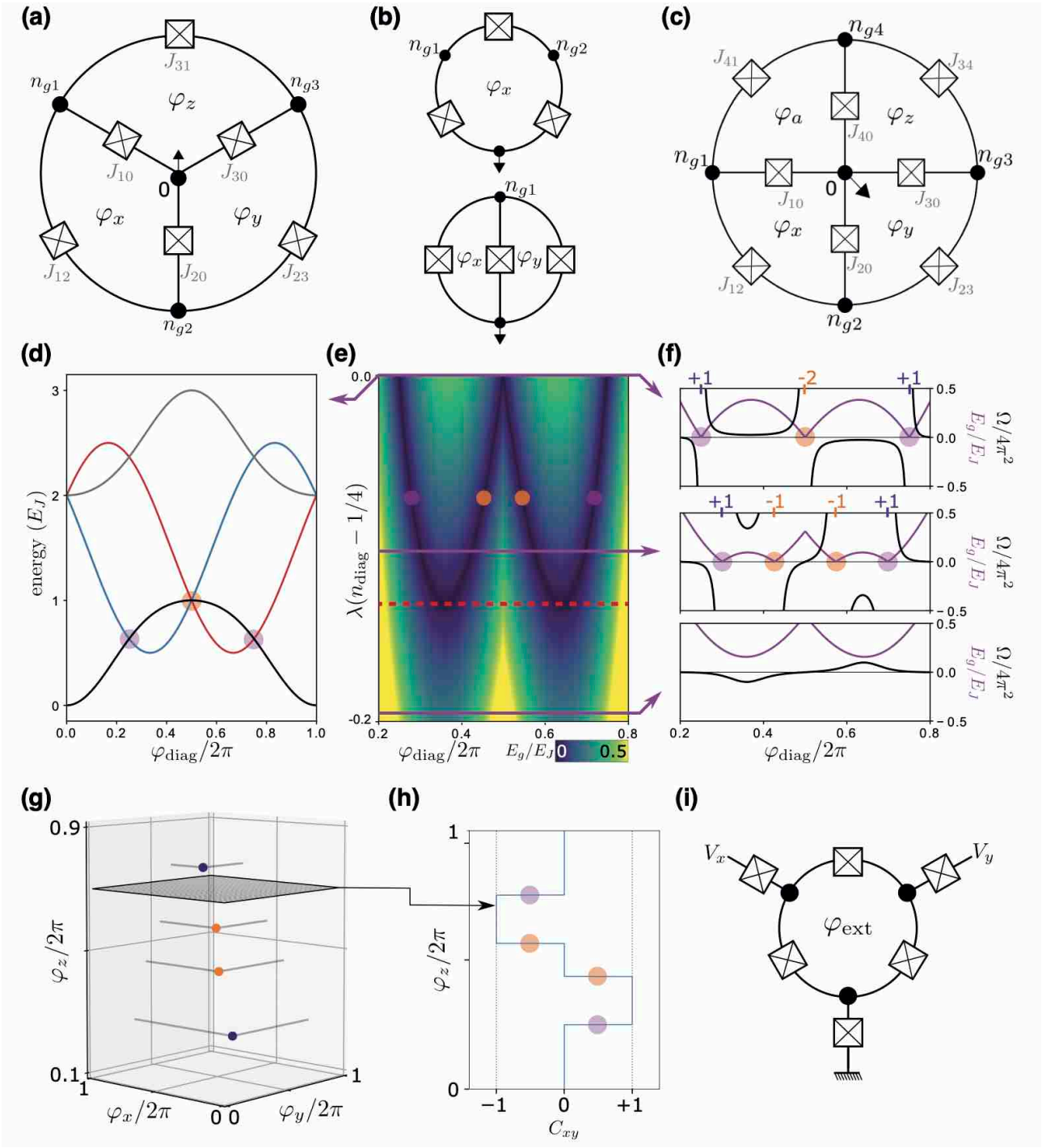

Fig. 14: Topological superconducting circuits. (a-c) Diagrams of 4 different Weyl Josephson circuits, composed of tunnel Josephson junctions and capacitances. Each node is labelled with its offset charge parameter n_{gi} and each loop is threaded by a reduced magnetic flux φ_j. **(d)** Energy spectrum as a function of diagonal flux at $\boldsymbol{n_g = n_{g0}}$. **(e)** Excitation gap as a function of diagonal flux and diagonal gate charge, exhibiting a topological phase transition (red dashed line) where Weyl nodes of opposite topological charge (purple and orange circles) annihilate. **(f)** Line cuts of the excitation gap (pink) and the Berry curvature (black) as a function of diagonal flux, for the indicated gate charge values. **(g)** Location of the Weyl nodes in the Brillouin zone, demonstrating like-charged nodes at opposite momenta. **(h)** Chern number as a function of φ_z. **(i)** Broken-open circuit for transconductance measurements.

To conclude, this work proposes a new approach to explore synthetic Weyl physics. It is based on standard superconducting circuits whose nanofabrication and measurement techniques are well mastered, allows for remarkably sophisticated, yet accessible, experiments. It should soon generate tangible experimental progress in the simulation of topological band structures. More generally, this work participates in the emergence of a new dynamic field of research, topological superconducting circuits, which merges the technological readiness and theoretical clarity of superconducting quantum circuits with the fundamental geometrical notions of topological condensed matter physics.

5.4 Andreev bound states in ultra-clean CNT based Josephson junctions

5.4.1 Objectives and experimental implementation

Superconducting qubits are intrinsically bosonic by nature as they rely on two macroscopic conjugated variables, namely the superconducting phase difference and the charge difference across the tunnel Josephson junction. Thus, traditional circuit Quantum Electrodynamics experiments somehow consist in measuring "the interplay between light and light". A promising direction involves leveraging mature cQED architectures and techniques to probe novel quantum systems and phenomena in well-controlled environments [26,142–144]. In particular, such an approach could allow one to probe and manipulate coherently novel quantum materials at the single fermion level and access the entanglement of condensed matter's elementary fermionic constituents. In addition to its fundamental interest, this line of research could make it possible to identify new elementary quantum systems favorable for quantum information processing.

Our research direction directly fits into this goal. It consists in engineering hybrid architectures combining superconducting circuits and low-dimensional conductors in order to isolate novel electronic states and manipulate their quantum states coherently (see Fig. 15a). More precisely, we want to probe and control the Andreev bound states in hybrid Josephson junctions. These microscopic fermionic states depend on the macroscopic superconducting phase difference across the junction. Thus, they naturally couple with superconducting photonic cavities and fit into cQED architectures. Although direct spectroscopic observations of ABS have recently been performed [13,23,90–92,145–147], their quantum properties were little explored and show limited coherence times [24,148–151]. Moreover, all these experiments were performed using either atomic break-junction or InAs semiconductor nanowires.

We chose to focus on ultra-clean carbon nanotubes (CNT). They are based on a new fabrication technique currently developed in our team (see Fig. 16), which allows for the growth, optical characterization and circuit integration of long straight disorder-free carbon nanotubes [152]. These pristine quantum conductors are intrinsically 1-dimensional objects (~ 1 nm-wide diameter). Therefore, they can host just a few ABS that can be controlled using local electrostatic gates (see Fig. 15c). Moreover, out of the ABS singularities, the electronic DOS vanishes below the superconducting gap (see Fig. 15d-e), which is essential for limiting decoherence and makes this material promising from a quantum point of view. Finally, owing to the CNT reduced dimensionality, electron-electron interactions play a crucial role in carbon nanotubes, which opens up great prospects in the context of many-body physics and quantum simulation.

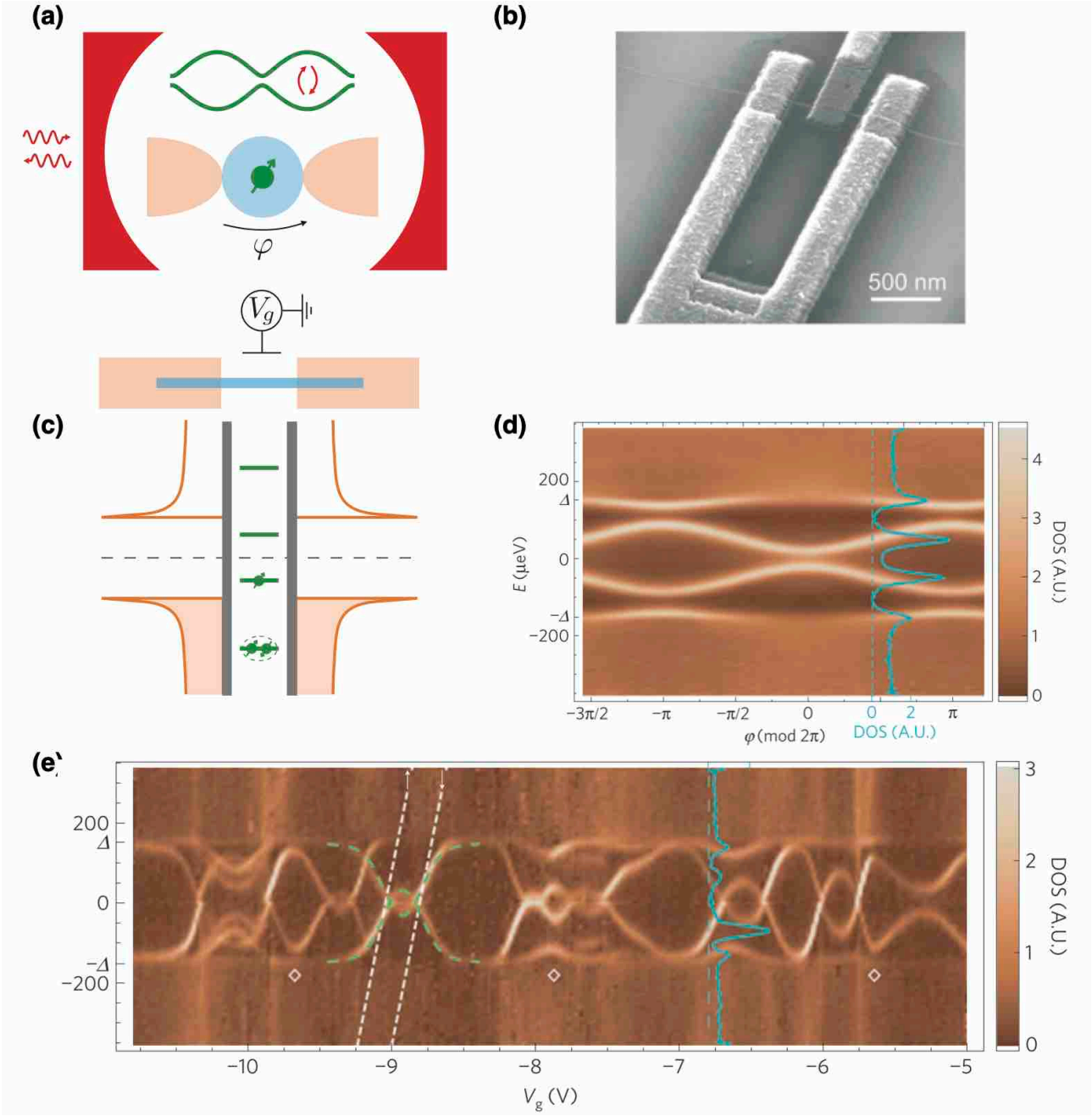

Fig 15: ABS in ultra-clean CNT based Josephson junction. (a, c) A single Andreev fermion is isolated within a hybrid Josephson junction – a carbon nanotube connected to two superconductors that behaves as a superconducting quantum dot. The Andreev spectrum depend both on the superconducting phase difference φ and on the gate voltage V_g. By enclosing the hybrid Josephson junction inside a superconducting photonic cavity, one can couple these fermionic states to microwave light and probe their quantum properties in a well-controlled environment. **(b)** SEM view of a carbon nanotube contacted to aluminum electrodes. **(d,e)** Phase-dependent and gate-dependent tunneling spectra of ABS within a proximitized carbon nanotube (data taken from Ref. [90]).

5.4.2 Growth, optical characterization and circuit integration of carbon nanotubes

The QCMX team is actively working on fabricating ultra-clean CNT-based devices. We have already performed several growths based on standard chemical vapor deposition technique, using the furnace of C12 in Paris, a start-up with whom we are collaborating. Recently, we have installed in our lab our own furnace (that can go up to 1200 °C), together with its gas handling system that allows to inject a controlled flow of argon, hydrogen and methane (see Fig. 16a), and we just did our first in-lab growths. The growth is performed using a custom-made silicon chip, with a 65 μm-wide and $\sim$3 mm-long slit that lies on a 50 μm-high raised platform (see top of Fig. 16b). A catalyst is deposited on one side of the slit such that nanotubes grow across it and end up being suspended (see Fig. 16b). This procedure naturally selects the cleanest CNT while allowing for subsequent imaging. Such a CNT, covered with 30 nm of Au, is shown in the optical picture of Fig. 16b.

In parallel, we have developed a home-made optical platform composed of a supercontinuum laser, a spectrometer, a camera, a microscope and a transfer station (see Fig. 16c). After a successful growth, a chip contains typically 3 to 10 suspended CNT distributed along the slit. By vertically placing the chip at the focal point of a microscope and illuminating the slit with the focused laser beam, we can locate the position of these CNT using a CCD camera (see Fig. 16d). This technique enables us to image a single macro-molecule that can be as narrow as 1 nm-wide for a single-wall CNT. Going further, we measure the Rayleigh scattering spectrum emitted by an individual CNT (or a bundle) using a broadband laser and a spectrometer. This allows us to identify the CNT's chirality and whether it is metallic or semiconducting, as illustrated in Fig. 16e. We typically look for spectra with just a few peaks (see Fig. 16h), to discard CNT bundles, and we select spectra corresponding to individual metallic CNT, as they yield better electrical contacts.

Once a promising CNT has been located and identified, we align it in-situ with the circuit chip where we have designed dedicated electrodes (see Fig. 16f) and applied a thin layer of resist except on the part where the CNT will be transferred. The integration of the CNT into the circuit is performed by mechanical transfer [153] similarly to what is done to make h-BN encapsulated graphene. The circuit chip is heated to soften the resist and then pressed on the growth chip to ensure a uniform mechanical contact between the resist and the slit that holds the CNT. The latter is then naturally grabbed by the resist and transferred to the circuit. The two chips are then slowly separated after cooling down to room temperature. Once the transfer is done, one can observe the chip using atomic force microscopy (see Fig. 16g).

Although this CNT nanofabrication technique is quite complex as it involves several steps, it increases drastically the yields by selecting individual long straight metallic CNT. More importantly, it allows for the production of ultra-clean CNT-based devices as the CNT are transferred as the last nanofabrication step. Although we are still struggling with the transfer, we recently managed to fabricate our first CNT device and performed low-frequency transport measurements at 10 mK. Fig. 16k shows the differential conductance as a function of both the bias voltage and the gate voltage. It exhibits well-known Coulomb diamonds, thus demonstrating quantum transport in a CNT. Their shape is however non-canonical, probably because we are observing a bundle of carbon nanotubes. Still, it is very promising and we should get soon better results once we have fully developed and mastered this ultra-clean CNT fabrication technique.

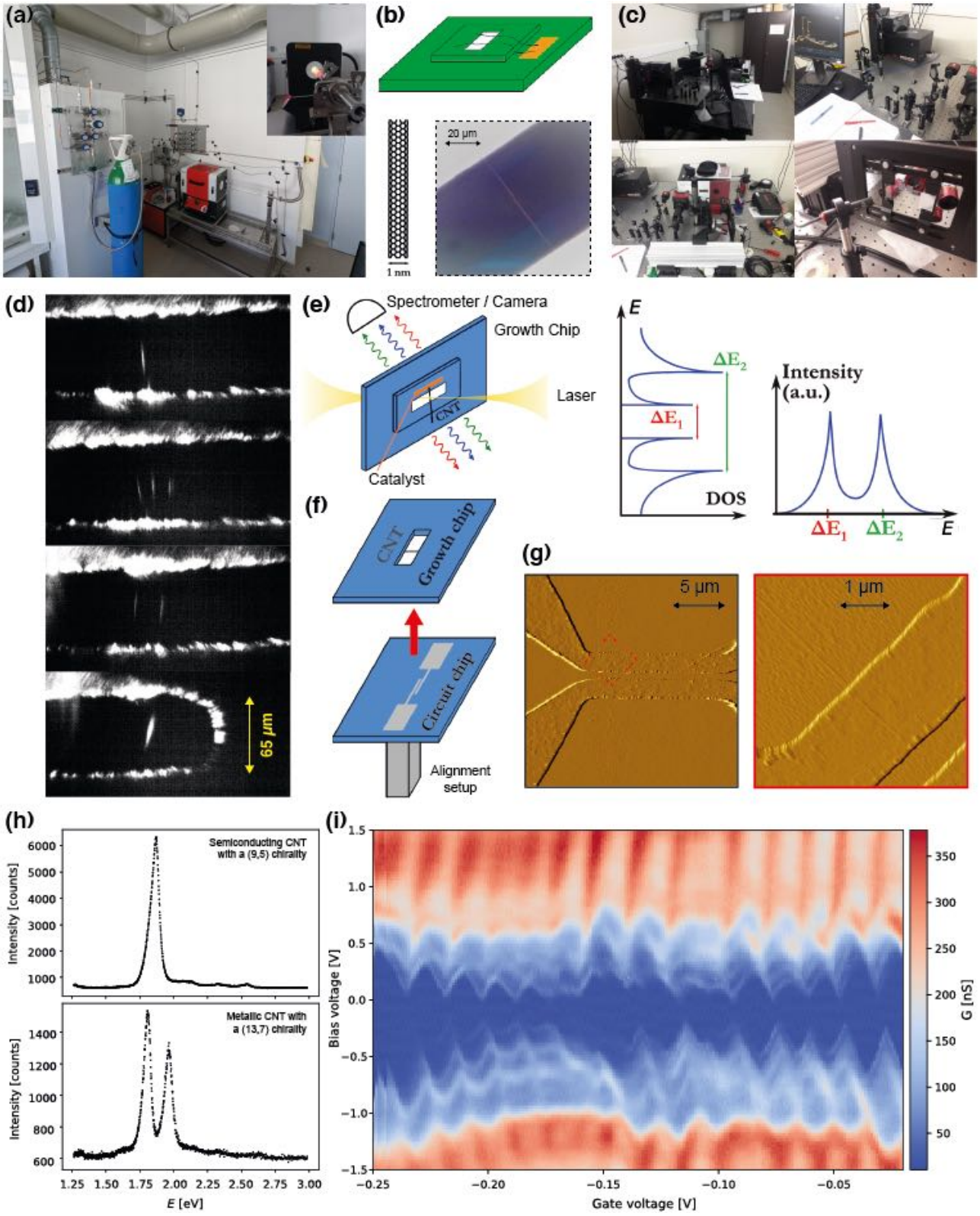

Fig 16: Growth, optical characterization and circuit integration of CNT. (a) Picture of the furnace and gas handling system. **(b)** Top: Schematic of the growth chip (green) with catalyst (orange) and suspended CNT. Bottom left: schematics of a mono-wall CNT. Bottom right: Optical picture of a CNT suspended over a 65 μm-wide slit and covered with gold. **(c)** Pictures of the optical platform. **(d)** Real-space imaging of CNT suspended ever a 65 μm-wide slit. **(e)** Schematics of the Rayleigh scattering spectroscopy. **(f)** Schematics of the mechanical transfer. **(g)** AFM pictures of the circuit chip after transfer exhibiting two Ti/Au electrodes and a single CNT. **(h)** 2 typical Rayleigh spectra, which allow to infer the CNT chirality. **(i)** Coulomb diamonds measurements at 10 mK: differential conductance of a CNT-based device as a function of both bias and gate voltages.

5.4.3 Two-tone Josephson spectroscopy

In parallel, we are developing a novel on-chip spectrometer in order to perform broad-band photonic spectroscopies of quantum systems hosted in mesoscopic devices, such as Andreev states in carbon nanotubes. This is a challenging task as their typical energy scales can be tuned between 0 and twice the superconducting gap. This results in a resonant frequency f_q that typically ranges between 1 GHz and 1 THz depending on the super-conductor used, which is out of range of all commercial radio-frequency instruments. Similarly to the work performed during my PhD (see section 2.2 and Ref. [13,14]), we chose here to exploit the AC Josephson effect to generate radiation at high frequency. However, the idea for this novel spectrometer is to separate the excitation from the detection. In "standard" Josephson spectroscopy [13,14,17–21,154,155], the detection is performed by measuring a relatively small DC current that flows through the Josephson junction emitter, which is sensitive to all of its electromagnetic environment including parasitic modes. Here instead, we use as a detector a microwave resonator whose resonant frequency lies in the range of cQED measurements (typically $f_c \sim 7$ GHz), with large quality factor ($Q \sim 10^4$), and which should be sensitive only to the system of interest.

Since it combines both AC Josephson effect and dispersive readout with a microwave cavity, we dubbed this novel technique "2-tone Josephson spectroscopy". Its principle is schematized in Fig. 17a. A quarter wavelength resonator is coupled to the quantum system under study, such as a CNT hosting ABS. The cavity resonant frequency f_c therefore depends on the state of the system owing to its non-linearity. The system is also coupled to a voltage-biased Josephson junction that behaves as an on-chip microwave emitter. It is biased at voltage V_J and irradiates photons at frequency $\nu_J = 2eV_J/h$. At resonance $\nu_J = f_q$, it induces transitions in the quantum system and the cavity resonant frequency is slightly shifted [24,137]. The detection is performed by probing the resonator via μwave reflectometry while sweeping the excitation frequency ν_J.

To validate this new approach, we are first trying to perform the spectroscopy of a "simple" quantum circuit, an RF-SQUID, *i.e.* a Josephson junction enclosed in a superconducting loop. It behaves as an anharmonic oscillator and its resonant frequency (typically targeted at $f_q \sim 100$ GHz) can be tuned with the flux threading the SQUID loop. Such a design is compatible with the later integration of a CNT-based hybrid Josephson junction (see Fig. 17e). In a first step, we worked on the detector and its coupling to the RF-SQUID, without any emitter. Fig. 17b shows the optical micrograph of a device with a $\lambda/4$ coplanar resonator made out of aluminum. It is inductively coupled to an RF-SQUID that contains an Al/Al_2O_3/Al tunnel Josephson junction (see Fig. 17c). We measured this cavity in reflection and could extract its resonant frequency ($f_c \sim 6.54$ GHz) and quality factors ($Q_{ext} \approx 3400$, $Q_{int} > 10^5$). Fig. 17d shows f_c as a function of the flux ϕ threading the SQUID loop. From the frequency modulation that shifts by $\delta f_c \approx 550$ kHz, we could infer a mutual inductance coupling of $M \approx 5$ pH, which is consistent with our Sonnet simulations.

Next, we started to work on the emitter part. We added to our previous design an Al/Al_2O_3/Al tunnel Josephson junction. Measuring in DC its current-voltage (IV) characteristics, we could extract its normal resistance $R_N = 2.3\,\mathrm{k\Omega}$ and switching current $I_S = 70\,\mathrm{nA}$. Then, we measured the cavity response while sweeping the voltage-bias on the junction emitter (see Fig. 17g). It exhibits a large frequency shift up to $\delta f_c \approx 8$ MHz, with no clear resonant feature that would correspond to the excitation of the RF-SQUID. We understood it is associated with the direct parasitic coupling between cavity and emitter. In this configuration, the cavity measures the complex impedance of the emitter, which is strongly voltage-dependent for a tunnel junction. In this measurement $f_c(V_b)$, we could indeed identify different regions that

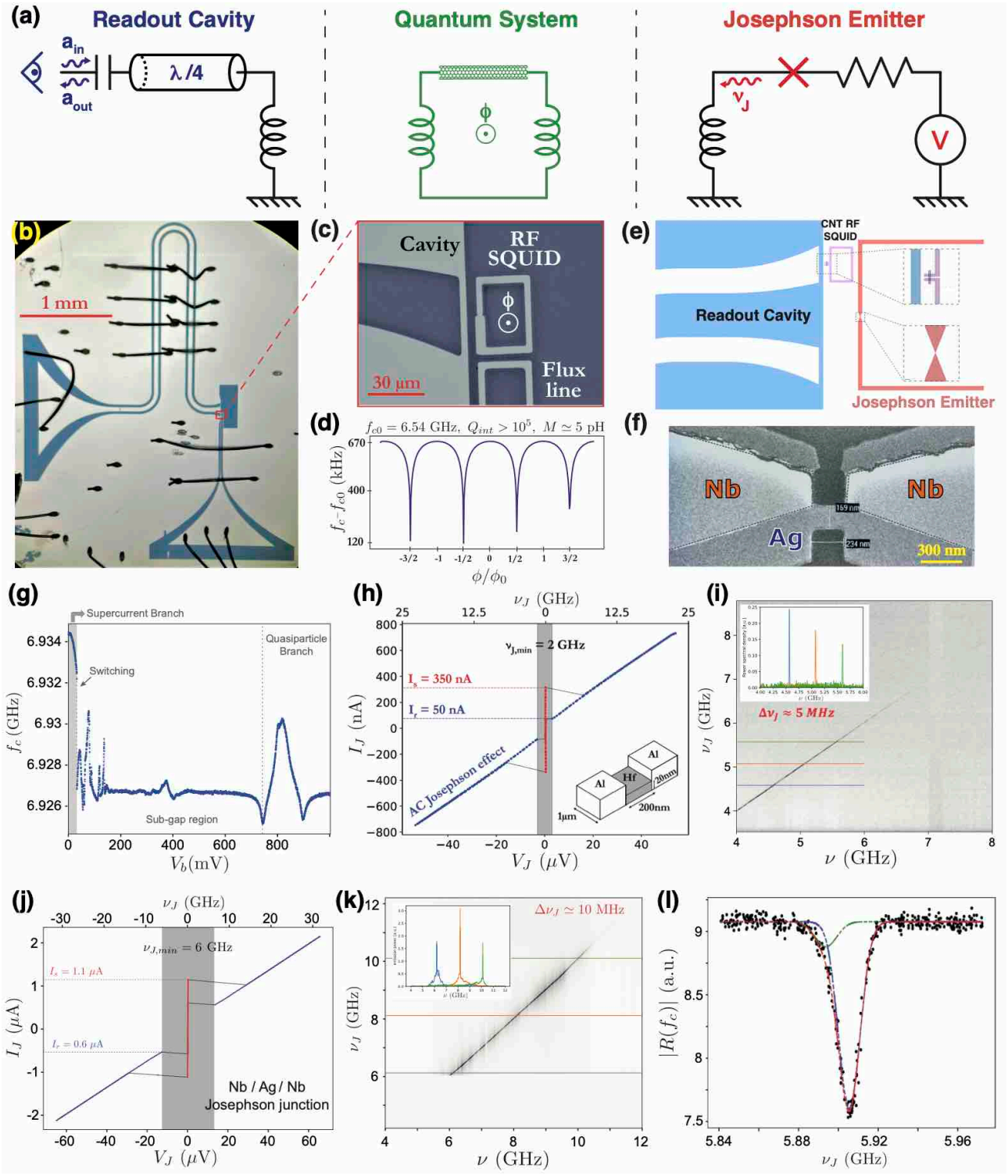

Fig 17: Two-tone Josephson spectroscopy. (a) Principle of the experiment. A voltage-biased Josephson junction is used as an emitter. It shines μwaves at frequency $\nu_J = 2eV_J/h$ towards a quantum system, such as a CNT hosting ABS. The latter is coupled to a μwave cavity, which is probed in reflectometry. When the quantum system is excited at resonance, the cavity resonant frequency f_c shifts, which enables the detection. **(b, c)** Optical micrographs of a preliminary device. An Al/Al_2O_3/Al tunnel Josephson junction is enclosed in a superconducting loop that is threaded by a magnetic flux ϕ, thus forming an RF SQUID. It is coupled both to a flux line and a $\lambda/4$ coplanar resonator. **(d)** Measured cavity resonant frequency f_c as a function of the flux ϕ. **(e)** Prospective design including both a $\lambda/4$ microwave cavity, a Josephson emitter and a CNT-based RF SQUID. This gradiometric geometry prevents to 1st order a direct coupling between the emitter and the cavity. **(f)** Scanning electron micrograph of a SNS Josephson junction made out of niobium and silver. **(g)** Cavity resonant frequency f_c as a function of the voltage applied on the Josephson emitter, which

is an Al/Al_2O_3/Al tunnel junction. **(h)** Current-voltage (IV) characteristic of an Al/Hf/Al Josephson junction with $I_S = 350$ nA and $\upsilon_{J,min} = 2$ GHz. **(i)** Gray-coded normalized power emitted by the same Al/Hf/Al junction, as a function of both the power spectrum analyzer measured frequency υ and the emitted Josephson frequency ν_J. Inset shows linecuts at different values of ν_J. **(j)** IV characteristic of an Nb/Ag/Nb SNS Josephson junction with $I_S = 1.1\,\mu$A and $\upsilon_{J,min} = 6$ GHz. **(k)** Gray-coded normalized power emitted by an Nb/Ag/Nb junction (same as in (f) and (j)), as a function of both υ and ν_J. Inset shows linecuts at different values of ν_J. **(l)** Black dots: spectrum of a transmon qubit measured using two-tone Josephson spectroscopy. Colored dashed lines: double gaussian fit of the absorption line.

correspond to the supercurrent branch, the sub-gap region and the quasiparticle branch. This measurement thus constitutes an alternative way to detect the voltage-dependent impedance $Z(V)$ of a conductor. This effect however completely dominates the readout and prevents us from implementing our two-tone Josephson spectroscopy. Tunnel junction emitters therefore suffer from having an impedance that is strongly voltage-dependent. On top of that, their intrinsic capacitance ($C_J \sim 75\,\mathrm{fF}/\mu\mathrm{m}^2$) shunts the Josephson radiation at high frequency, with a cutoff frequency that varies typically between 10 and 50 GHz.

To circumvent these problems, we decided to use a Superconductor-Normal-Superconductor (SNS) Josephson junction as an emitter. Indeed, since its IV characteristic is almost linear at finite voltage and its intrinsic capacitance is very small, it should behave as a classical ac current source up to large frequency. Using optical lithography, we fabricated an Al/Hf/Al junction with a 200 nm-long, 1 μm-large, and 20 nm-thick central region made out of hafnium (Hf) in order to benefit from its large resistivity. Fig. 17h shows the IV characteristics of such a junction, which exhibits a switching current $I_S = 350$ nA, a retrapping current $I_R = 50$ nA and a normal resistance $R_N = 80\,\Omega$. The retrapping-voltage translates into a minimum Josephson frequency $\upsilon_{J,min} = 2$ GHz. To characterize further the junction, we measured the microwave emission associated with the AC Josephson effect. Using a bias-tee (with cutoff frequency 70 kHz), we could channel the Josephson radiation on a microwave detection line consisting in a 4-8 GHz band-pass filter, a 4-12 GHz dual isolator, an NbTi coaxial line, a 4-16 GHz cryogenic low-noise amplifier and a power spectrum analyzer. Thus, we could measure the RF power emitted by the junction as a function of frequency ν, while sweeping the voltage-controlled Josephson frequency $\nu_J = 2eV_J/h$ (see Fig. 17i). We observe a narrow peak centered at $\nu = \nu_J$ that varies linearly with the voltage, thus demonstrating AC Josephson emission. Moreover, linecuts reveal a very small emission width $\Delta\nu_J = 5$ MHz comparable to state-of-the art experiments [156]. They originate from fluctuations of the bias voltage at low frequency, which were heavily filtered using a dedicated bias-box fabricated at SPEC by Patrice Jacques.

Although these measurements were promising, the AC supercurrent was much smaller than the DC supercurrent. Varying the junction dimensions, we realized that the AC supercurrent at finite voltage was associated with proximity effect while the DC supercurrent at zero voltage was dominated by hafnium intrinsic superconductivity. Therefore, we decided to switch to Nb/Ag/Nb SNS junctions where the weak link is made out of silver (Ag), which is a normal metal at 10 mK. These niobium-based Josephson junction emitters are very promising as they should allow for experiments in the THz range, owing to Nb larger superconducting gap. Fig. 17f shows the scanning electron micrograph of such an Nb/Ag/Nb SNS junction, which we fabricated using e-beam lithography, with a normal weak link being 230 nm-long, 170 nm-large, and 30 nm-thick. Fig. 17j shows the IV characteristics of this junction, which exhibits a switching current $I_S = 1.1\,\mu$A, a retrapping current $I_R = 600$ nA, a normal resistance $R_N = 30\,\Omega$ and a minimum Josephson frequency $\upsilon_{J,min} = 6$ GHz. Using a similar setup as before, we measured the RF power emitted by the junction as a function of

both measured frequency ν and Josephson frequency ν_J (see Fig. 17k). It displays a voltage-tunable Josephson emission peak centered at $\nu = \nu_J$, with a narrow width $\Delta\nu_J = 10$ MHz. It is twice larger than before, which we attribute to a small change of the microwave environment seen by the junction.

Next, we did an experiment by combining our Al/Hf/Al junction emitter with a separated device that contains a transmon qubit coupled to a microwave cavity (see details in section 5.4.4). We used these to demonstrate the principle of two-tone Josephson spectroscopy, with the qubit behaving as the quantum system of interest and the microwave cavity as the detector. We channeled the Josephson radiation emitted by the Al/Hf/Al junction towards the transmon device while measuring in reflection the cavity close to its resonant frequency $f_c \approx 8.178$ GHz. Fig. 17l shows such a measurement as a function of the emitted Josephson frequency ν_J. We observe a dip in the reflection amplitude at frequency $\nu_J \approx 5.906$ GHz. We interpret it as the resonant absorption by the qubit at frequency $f_q \approx 5.906$ GHz, which shifts the cavity frequency. In practice, the absorption line finesse is limited by the Josephson emission width $\Delta\nu_J = 5$ MHz, which is comparable with the dispersion interaction between the qubit and the cavity $\chi = 10.7$ MHz (see section 5.4.4). Therefore, the absorption line is composed of the two transitions $|g,0\rangle \rightarrow |e,0\rangle$ and $|g,1\rangle \rightarrow |e,1\rangle$, which correspond to the excitation of the qubit with either 0 or 1 (thermal) photon in the cavity and are resonant at frequencies f_q and $f_q - \chi$ (see section 3.4). We could fit the absorption line with two weighted gaussians (colored dashed lines in Fig. 17l). From the ratio of the peak heights, we infer an occupation of the cavity of ~ 0.1 photon, which corresponds to an effective temperature of ~ 90 mK. This experiment constitutes the first implementation of two-tone Josephson spectroscopy though it is realized to detect a well-known quantum circuit that resonates at low frequency. We are now designing and fabricating a complete device that integrates both a detector, an SNS junction emitter and a non-linear cavity with resonant modes at high frequency. Next, we will use our newly developed spectrometer with a CNT-based hybrid Josephson junction (see Fig. 17e) to perform the photonic spectroscopy of ABS in ultra-clean CNT. We plan to explore different regimes for the carbon nanotube, either in single-dot or double-dots configurations. Such a measurement should be very different from what is obtained via tunnel spectroscopy [90,91] as photon excitation induces transition that conserves parity without paying the charging energy.

5.4.4 Towards quantum measurement and control of ABS in a cQED architecture

Going further, we plan to investigate the quantum properties of the Andreev states in ultra-clean CNT-based hybrid Josephson junctions. As before, the Andreev spectrum will be tuned by using both local electrostatic gates and magnetic fluxes, the latter being enabled by enclosing the hybrid junction in a superconducting loop, thus forming an RF-SQUID. On top of that, we will use state-of-the-art circuit quantum electrodynamics architectures and techniques to observe and manipulate the Andreev states (see Fig. 15a and Fig. 19a). These architectures indeed provide a well-controlled electromagnetic environment and help protect the qubits from decoherence. By coupling the hybrid Josephson junction to a photonic cavity, we will manipulate the Andreev qubit and measure its state using microwaves. Based on the intrinsic low-dimensional properties of carbon nanotubes and the high-quality of our fabrication procedure in which the nanotubes are transferred at the last step and have seen no resist, we expect to implement long-lived Andreev qubits.

To prepare for quantum coherence measurements in the time-domain, we have purchased and installed multiple μwave instruments, including a vectorial network analyzer, microwave sources, cryogenic low-noise amplifiers and a quantum orchestration platform from Quantum Machines that is needed for pulsing, demodulating and measuring the μwave

signals. As a first step, and to validate our measurement setup, we have performed several cQED experiments using a transmon qubit as a system of interest. It was designed and nanofabricated by Léo Balembois, who is doing a PhD at SPEC under the supervision of Emmanuel Flurin. The qubit is based on a standard aluminum tunnel junction with Josephson energy $E_J/h \sim 16.4$ GHz and a shunt capacitor with energy $E_C/h \sim 266$ MHz. The qubit thus operates in the transmon regime $E_J \gg E_c$ where it is insensitive to charge noise [35]. It is coupled to a high-Q coplanar resonator made out of tantalum, through a large-band Purcell filter. The transmon chip was fabricated on a sapphire substrate and mounted in a JAWS sample-holder that was designed and manufactured by Marius Villiers, who is doing a PhD at ENS under the supervision of Zaki Leghtas.

We have characterized this device at 10 mK. We first measured the microwave reflection of the resonator as a function of the readout frequency (see blue curve in Fig. 18a), which exhibits a resonance at $f_c \approx 8.178$ GHz with quality factors $Q_{ext} \approx 5000$ and $Q_{int} \approx 43000$. Next, we performed a two-tone spectroscopy and could extract the qubit resonant frequency $f_q \approx 5.91$ GHz and its anharmonicity $\alpha \approx 266\,\mathrm{MHz}$, which allowed us to infer E_J and E_C. When driving the qubit at resonance for a long time, the qubit reaches the maximally mixed state $(|g\rangle\langle g| + |e\rangle\langle e|)/2$. Consequently, the resonator spectrum is modified (see orange curve in Fig. 18a) and a second deep appears at $f_c - \chi$, which corresponds to the qubit being in the excited state $|e\rangle$. This bipartite qubit-cavity system is described by the same Hamiltonian discussed in section 3:

$$H/h = f_q|e\rangle\langle e| + f_c a^\dagger a - \chi|e\rangle\langle e|a^\dagger a$$

with a dispersive shift interaction measured to be $\chi = 10.7$ MHz.

Going further, we have probed the qubit quantum coherence by performing operations in the time domain. First, we probed the resonator spectrum after exciting the qubit at resonance with a pulse whose duration was varied (see Fig. 18b). The resonator spectrum exhibits a Rabi swing as a function of the driving-pulse duration, with out-of-phase oscillations at f_c and $f_c - \chi$, demonstrating coherent oscillations between the qubit states $|g\rangle$ and $|e\rangle$. The strong coupling between qubit and cavity allows one to perform single-shot measurements of the qubit state. We could thus measure the probability $P_{|e\rangle}$ of the qubit to be in the excited state as a function of time. Such a measurement is shown in Fig. 18c while driving the qubit at resonance, and exhibits Rabi oscillations with a frequency $\Omega_R \approx 0.5$ MHz and a damping time $T_R \approx 19$ μs. We performed a similar measurement, where we varied in addition the qubit drive frequency, resulting in the well-known Rabi chevrons (see Fig. 18d).

Using Rabi oscillations, one can calibrate a π-pulse (respectively $\pi/2$-pulse), which rotates the qubit state in the Bloch sphere about the x-axis by an angle π (resp. $\pi/2$). Thus, by applying a π-pulse that prepares the qubit in state $|e\rangle$, we could measure after a variable delay an exponential decay trace with an energy relaxation time $T_1 \approx 40$ μs (Fig. 18e). Finally, we have used Ramsey interferometry technique to measure the dephasing for an equal qubit superposition $(|g\rangle + |e\rangle)/\sqrt{2}$. It consists in the application of two $\pi/2$-pulses detuned at $f_d - f_q \approx 1$ MHz and separated by a varying delay time. Fig. 18f shows the corresponding Ramsey oscillations, which indicate coherent precession of the qubit state in the Bloch sphere around the z-axis. From the decay, we could extract a dephasing time $T_2^* \approx 16$ μs. This value being much smaller than $2T_1$, our qubit coherence is dominated by pure dephasing with a characteristic time $T_\varphi \approx 20$ μs.

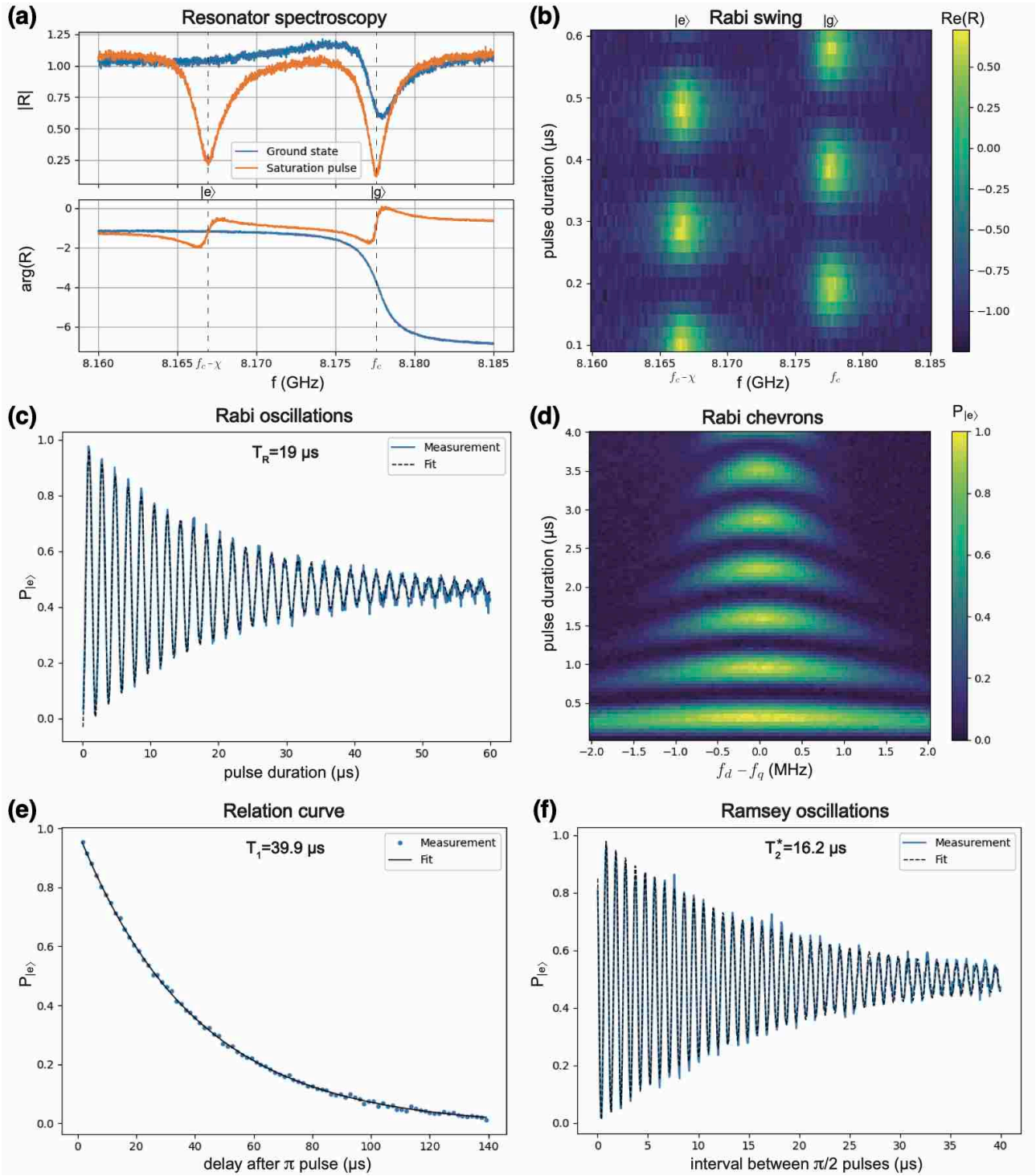

Fig 18: Quantum control & measurement of a superconducting transmon qubit. (a) Resonator spectrum: reflection amplitude as a function of frequency for the qubit in the ground state (blue curve) and in an excited mixed state following a saturation pulse at the qubit resonant frequency (orange curve). **(b)** Rabi swing: resonator spectrum, when driving the qubit at resonance at $f_q \approx 5.91$ GHz, as a function of the driving-pulse duration. **(c)** Rabi oscillations: qubit population as a function of the driving-pulse duration. The fitting yields $\Omega_R \approx 0.5$ MHz and $T_R \approx 19$ μs. **(d)** Rabi chevrons: Rabi oscillations as a function of the qubit drive detuning frequency. **(e)** T_1 relaxation curve: qubit population as a function of delay time after a π-pulse, which was calibrated from the Rabi oscillations. The fitting to an exponential decay yields $T_1 \approx 40$ μs. **(f)** Ramsey fringes: qubit population as a function of delay between two $\pi/2$-pulses detuned at $f_d - f_q \approx 1$ MHz. The fitting yields $T_2^* \approx 16$ μs.

5.4.5 Carbon nanotube-based bosonic superconducting qubits

In addition to Andreev's fermionic microscopic degree of freedom, each hybrid Josephson junction has a macroscopic degree of freedom associated with the phase and charge differences. When combined with a parallel capacitance (intrinsic or added), a Josephson junction behaves as an anharmonic oscillator whose first two levels can be used as a bosonic superconducting qubit. Its frequency can be varied by electrostatically controlling the Andreev spectrum, as already demonstrated using semiconducting nanowires in so-called *gatemons* [114–116]. Using a CNT as the weak link will enable a low-enough Josephson energy E_J so that the qubit frequency f_q is in a range measurable by cQED techniques (~ 2-20 GHz). We plan to use a hybrid Josephson junction without a loop and operate it at $\langle\varphi\rangle = 0$ (see bottom left qubit in Fig. 19a). The energy of the ABS is then huge and this microscopic degree of freedom is frozen. In parallel with the junction, a large shunt capacitance (rectangular metal island in Fig. 19a) is placed to operate the qubit in the transmon regime $(E_J/E_C \sim 50 - 100)$, to minimize the effect of charge noise and quasiparticle jumps [35]. Once again, we hope to implement long-lived qubits owing to our ultra-clean CNT fabrication procedure.

Next, we plan to explore a different configuration: a SQUID consisting of a hybrid Josephson junction in parallel with a large Josephson tunnel junction. The total Josephson energy of this SQUID can be controlled by the magnetic flux ϕ applied through the loop. At $\phi = 0$, the Josephson energy of the tunnel junction dominates and the system behaves as a standard transmon. At $\phi = \pi$, the Josephson potential is strongly modified. By increasing the Josephson energy of the weak link using the gate voltage, the potential in the phase space evolves from a simple quadratic well to a double well through a quartic potential (see Fig. 19b). This system is very rich and will allow for the implementation of a bosonic qubit whose properties (resonant frequency, anharmonicity) can be greatly modified. In particular, it should be possible to obtain large coherence times in the quartic configuration [157] and engineer a lambda system.

Going further, by using the same system and tuning properly the gate voltage and magnetic flux, one can in principle place the bosonic and fermionic qubits close to resonance, so that they naturally couple and hybridize (see lower graph of Fig. 19b). We plan to study the entanglement of these two very different degrees of freedom (micro vs. macroscopic, fermionic vs. bosonic) and observe the joint quantum dynamics of this spin-boson system. This elementary system will play the role of a quantum simulator and allow us to understand better the spin-boson model, which is at the heart of the description of dissipation in quantum physics [158]. Finally, we would like to investigate another promising system, a symmetrical SQUID consisting of two hybrid Josephson junctions in parallel. Indeed, by properly gate-tuning each CNT-based junction, one could in principle implement a $\cos(2\varphi)$ Josephson junction, which is π-periodic in phase. It is predicted that such a system could be used as a topologically protected qubit [159].

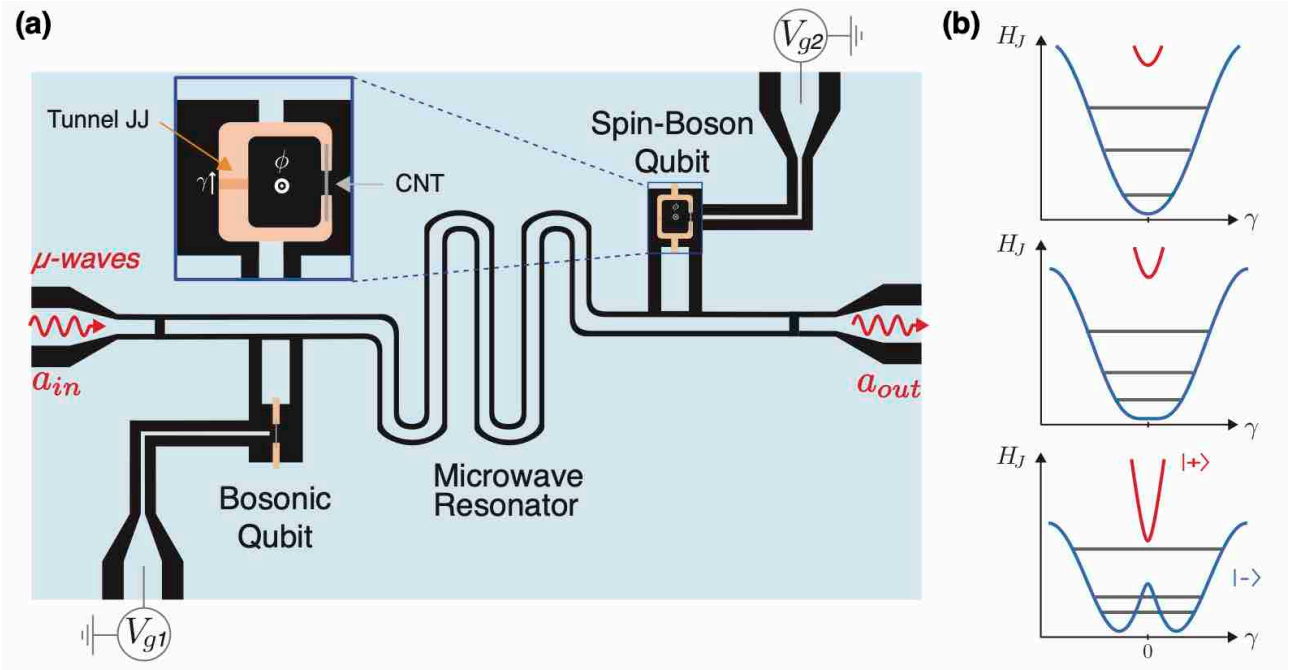

Fig 19: Carbon nanotube-based bosonic superconducting qubits. (a) Typical design of a hybrid cQED architecture. CNT-based Josephson junctions behave as superconducting qubits and are capacitively coupled to a $\lambda/2$ resonator. These qubits can be controlled independently with gate voltages and magnetic fluxes. The bottom left device - a single CNT-based junction - implements a bosonic qubit that operates at $\langle\varphi\rangle = 0$. The upper right device (zoom in inset) - a SQUID consisting of a CNT-based junction in parallel with a Josephson tunnel junction – implements a more versatile and exotic quantum system. **(b)** Josephson energy potential of a single-channel Josephson weak link with transmission τ, in parallel with a tunnel Josephson function. It is plotted as a function of the superconducting phase difference, at flux $\phi = \pi$, with the Andreev doublet either in the ground state (blue line) or excited state (red line). By tuning the transmission τ, the Andreev spectrum is modified and one can change the effective energy potential from a simple to a double well. This allows for the implementation of an extremely versatile bosonic qubit, as schematized with the quantized energy levels (grey lines). At large transmission $\tau \to 1$, the Andreev transition is at low energy so that fermionic and bosonic qubits have close energies and get entangled.

6 Perspectives

The hybrid architectures that we are developing, which combine quantum conductors and superconducting photonic cavities, are very flexible and have huge potential in terms of complexity and control. They constitute unique platforms to perform experiments at the boundary between condensed matter physics and microwave quantum optics.

First, the physics we explore naturally connect to the quest for detecting Majorana fermions [160]. These non-abelian particles are indeed predicted to form in hybrid Josephson junctions following a topological phase transition [161–164]. In this context, they can be thought as very exotic ABS. Despite some experimental progress using semi-conducting heterostructures [146,161], there is still a critical need for exploring further this physics. CNT-based Josephson junction could provide an alternative path, as they are predicted to host helical modes in presence of a large perpendicular electric field [162,163], which could be done by using hBN as a dielectric layer.

Our systems are also good candidates to probe fundamental phenomena, such as light-matter interaction in the non-equilibrium regime. Indeed, I believe it would be very interesting to detect the quantum properties of the microwave light emitted by a voltage-biased quantum conductor, associated with the inelastic transport of Cooper pairs [22,156,164,165]. On the other hand, such hybrid quantum circuits could also be used to study decoherence mechanisms in quantum materials, in particular the effects associated with the specific interactions and symmetries of their electronic band structure [166].

On a broad picture, these architectures have great potential for analog quantum simulation. As envisioned by Richard Feynman, one could use a network of quantum bits or resonators to simulate and solve complex many-body problems. Using microscopic fermions isolated in quantum conductors as elementary bricks is particularly promising owing to their different quantum statistic and their inclination to interact via Coulomb repulsion.

Finally, we are also willing to investigate different systems that do not necessarily involve carbon nanotubes. In particular, we are currently developing aluminum-based pinhole Josephson junctions, which host just a few well-transmitted channels that dominate the supercurrent. They could allow us to explore Andreev physics from a different angle, with some promising prospects related to non-local Josephson effect and Andreev molecules [167]. We are also interested to explore the emerging field of topological Josephson quantum circuits where one can simulate Weyl semi-metal band-structures with non-trivial topology using standard tunnel Josephson junctions [123,138].

Although it is always difficult in research to predict what will happen tomorrow, it is fair to assume that all this development will enable lots of exciting and various activities in the nascent field of hybrid quantum circuits.

References

[1] B. D. Josephson, Phys. Lett. **1**, 251 (1962).

[2] A. F. Andreev, Sov Phys JETP **19**, 1228 (1964).

[3] D. Saint-James, J. Phys. Fr. **25**, 899 (1964).

[4] I. O. Kulik, Sov. Phys. JETP **30**, 944 (1970).

[5] L. Bretheau, Ç. Girit, L. Tosi, M. Goffman, P. Joyez, H. Pothier, D. Esteve, and C. Urbina, Comptes Rendus Phys. **13**, 89 (2012).

[6] A. Furusaki and M. Tsukada, Solid State Commun. **78**, 299 (1991).

[7] C. W. J. Beenakker and H. van Houten, Phys. Rev. Lett. **66**, 3056 (1991).

[8] P. F. Bagwell, Phys. Rev. B **46**, 12573 (1992).

[9] G. Wendin and V. S. Shumeiko, Superlatt. and Microstruct. **20**, 569 (1996).

[10] M. Zgirski, L. Bretheau, Q. Le Masne, H. Pothier, D. Esteve, and C. Urbina, Phys. Rev. Lett. **106**, 257003 (2011).

[11] D. G. Olivares, A. Levy Yeyati, L. Bretheau, Ç. Ö. Girit, H. Pothier, and C. Urbina, Phys. Rev. B **89**, 104504 (2014).

[12] M. L. Della Rocca, M. Chauvin, B. Huard, H. Pothier, D. Esteve, and C. Urbina, Phys. Rev. Lett. **99**, 127005 (2007).

[13] L. Bretheau, Ç. Ö. Girit, H. Pothier, D. Esteve, and C. Urbina, Nature **499**, 312 (2013).

[14] L. Bretheau, Ç. Girit, M. Houzet, H. Pothier, D. Esteve, and C. Urbina, Phys. Rev. B **90**, 134506 (2014).

[15] A. H. Dayem and C. C. Grimes, Appl. Phys. Lett. **9**, 47 (1966).

[16] G.-L. Ingold and Y. V. Nazarov, in *Single Charg. Tunneling*, edited by M. D. H. Grabert (Plenum Press, New York, 1992), pp. 21–107.

[17] J. Edstam and H. K. Olsson, Appl. Phys. Lett. **64**, 2733 (1994).

[18] R. Lindell, J. Penttilä, M. Sillanpää, and P. Hakonen, Phys. Rev. B - Condens. Matter Mater. Phys. **68**, 2 (2003).

[19] J. Leppäkangas, E. Thuneberg, R. Lindell, and P. Hakonen, Phys. Rev. B **74**, 054504 (2006).

[20] P.-M. Billangeon, F. Pierre, H. Bouchiat, and R. Deblock, Phys. Rev. Lett. **98**, 126802 (2007).

[21] J. Basset, H. Bouchiat, and R. Deblock, Phys. Rev. B - Condens. Matter Mater. Phys. **85**, 1 (2012).

[22] M. Hofheinz, F. Portier, Q. Baudouin, P. Joyez, D. Vion, P. Bertet, P. Roche, and D. Esteve, Phys. Rev. Lett. **106**, 217005 (2011).

[23] L. Bretheau, Ç. Ö. Girit, C. Urbina, D. Esteve, and H. Pothier, Phys. Rev. X **3**, 041034 (2013).

[24] C. Janvier, L. Tosi, L. Bretheau, Ç. Ö. Girit, M. Stern, P. Bertet, P. Joyez, D. Vion, D. Esteve, M. F. Goffman, H. Pothier, and C. Urbina, Science **349**, 1199 (2015).

[25] L. Bretheau, Localized Excitations in Superconducting Atomic Contacts : Probing the Andreev Doublet, 2013.

[26] R. J. Schoelkopf and S. M. Girvin, Nature **451**, 664 (2008).

[27] A. Wallraff, D. I. Schuster, A. Blais, L. Frunzio, J. Majer, S. Kumar, S. M. Girvin, and R. J. Schoelkopf, Nature **431**, 162 (2004).

[28] S. Haroche and J.-M. Raimond, *Exploring the Quantum: Atoms, Cavities, and Photons* (Oxford Graduate Texts, 2006).

[29] J. M. Raimond, M. Brune, and S. Haroche, Rev. Mod. Phys. **73**, 565 (2001).

[30] J. Clarke and F. K. Wilhelm, Nature **453**, 1031 (2008).

[31] M. H. Devoret and R. J. Schoelkopf, Science **339**, 1169 (2013).

[32] N. Roch, E. Flurin, F. Nguyen, P. Morfin, P. Campagne-Ibarcq, M. H. Devoret, and B. Huard, Phys. Rev. Lett. **108**, 147701 (2012).

[33] E. Flurin, N. Roch, F. Mallet, M. H. Devoret, and B. Huard, Phys. Rev. Lett. **109**, 183901 (2012).

[34] P. Campagne-Ibarcq, E. Flurin, N. Roch, D. Darson, P. Morfin, M. Mirrahimi, M. H. Devoret, F. Mallet, and B. Huard, Phys. Rev. X **3**, 021008 (2013).

[35] J. Koch, T. M. Yu, J. Gambetta, A. A. Houck, D. I. Schuster, J. Majer, A. Blais, M. H. Devoret, S. M. Girvin, and R. J. Schoelkopf, Phys. Rev. A **76**, 042139 (2007).

[36] H. Paik, D. I. Schuster, L. S. Bishop, G. Kirchmair, G. Catelani, A. P. Sears, B. R. Johnson, M. J. Reagor, L. Frunzio, L. I. Glazman, S. M. Girvin, M. H. Devoret, and R. J. Schoelkopf, Phys. Rev. Lett. **107**, 240501 (2011).

[37] P. Campagne-Ibarcq, L. Bretheau, E. Flurin, A. Auffèves, F. Mallet, and B. Huard, Phys. Rev. Lett. **112**, 180402 (2014).

[38] H. Wiseman, Phys. Rev. A **65**, 032111 (2002).

[39] M. Tsang, Phys. Rev. A - At. Mol. Opt. Phys. **80**, 1 (2009).

[40] S. Gammelmark, B. Julsgaard, and K. Mølmer, Phys. Rev. Lett. **111**, 160401 (2013).

[41] O. Astafiev, a M. Zagoskin, a a Abdumalikov, Y. a Pashkin, T. Yamamoto, K. Inomata, Y. Nakamura, and J. S. Tsai, Science **327**, 840 (2010).

[42] Y. Aharonov, D. Albert, and L. Vaidman, Phys. Rev. Lett. **60**, 1351 (1988).

[43] N. Ritchie, J. Story, and R. Hulet, Phys. Rev. Lett. 1107 (1991).

[44] A. Palacios-Laloy, F. Mallet, F. Nguyen, P. Bertet, D. Vion, D. Esteve, and A. N. Korotkov, Nat. Phys. **6**, 442 (2010).

[45] J. P. Groen, D. Ristè, L. Tornberg, J. Cramer, P. C. de Groot, T. Picot, G. Johansson, and L. DiCarlo, Phys. Rev. Lett. **111**, 090506 (2013).

[46] P. Campagne-Ibarcq, P. Six, L. Bretheau, A. Sarlette, M. Mirrahimi, P. Rouchon, and B. Huard, Phys. Rev. X **6**, 011002 (2016).

[47] P. Campagne-Ibarcq, S. Jezouin, N. Cottet, P. Six, L. Bretheau, F. Mallet, A. Sarlette, P. Rouchon, and B. Huard, Phys. Rev. Lett. **117**, 1 (2016).

[48] H. M. Wiseman and G. J. Milburn, *Quantum Measurement and Control* (2010).

[49] H. M. Wiseman and G. J. Milburn, Phys. Rev. A **47**, 1652 (1993).

[50] R. Vijay, D. H. Slichter, and I. Siddiqi, Phys. Rev. Lett. **106**, 110502 (2011).

[51] K. W. Murch, S. J. Weber, C. Macklin, and I. Siddiqi, Nature **502**, 211 (2013).

[52] M. Hatridge, S. Shankar, M. Mirrahimi, F. Schackert, K. Geerlings, T. Brecht, K. M. Sliwa, B. Abdo, L. Frunzio, S. M. Girvin, R. J. Schoelkopf, and M. H. Devoret, Science **339**, 178 (2013).

[53] P. Campagne-Ibarcq, Measurement Back Action and Feedback in Superconducting Circuits, 2015.

[54] M. M. Desjardins, J. J. Viennot, M. C. Dartiailh, L. E. Bruhat, M. R. Delbecq, M. Lee, M. S. Choi, A. Cottet, and T. Kontos, Nature **545**, 71 (2017).

[55] L. Bretheau, P. Campagne-Ibarcq, E. Flurin, F. Mallet, and B. Huard, Science **348**, 776 (2015).

[56] P. Facchi, V. Gorini, G. Marmo, S. Pascazio, and E. C. G. Sudarshan, Phys. Lett. A **275**, 12 (2000).

[57] P. Facchi and S. Pascazio, Phys. Rev. Lett. **89**, 080401 (2002).

[58] P. Facchi, D. Lidar, and S. Pascazio, Phys. Rev. A **69**, 032314 (2004).

[59] J. M. Raimond, C. Sayrin, S. Gleyzes, I. Dotsenko, M. Brune, S. Haroche, P. Facchi, and S. Pascazio, Phys. Rev. Lett. **105**, 213601 (2010).

[60] J. M. Raimond, P. Facchi, B. Peaudecerf, S. Pascazio, C. Sayrin, I. Dotsenko, S. Gleyzes, M. Brune, and S. Haroche, Phys. Rev. A **86**, 032120 (2012).

[61] F. Schäfer, I. Herrera, S. Cherukattil, C. Lovecchio, F. S. Cataliotti, F. Caruso, and A. Smerzi, Nat. Commun. **5**, 3194 (2014).

[62] A. Signoles, A. Facon, D. Grosso, I. Dotsenko, S. Haroche, J.-M. Raimond, M. Brune, and S. Gleyzes, Nat. Phys. **10**, 715 (2014).

[63] L. Lutterbach and L. Davidovich, Phys. Rev. Lett. **78**, 2547 (1997).

[64] P. Bertet, a. Auffeves, P. Maioli, S. Osnaghi, T. Meunier, M. Brune, J. Raimond, and S. Haroche, Phys. Rev. Lett. **89**, 200402 (2002).

[65] B. Vlastakis, G. Kirchmair, Z. Leghtas, S. E. Nigg, L. Frunzio, S. M. Girvin, M. Mirrahimi, M. H. Devoret, and R. J. Schoelkopf, Science **342**, 607 (2013).

[66] K. S. Novoselov, A. K. Geim, S. V. Morozov, D. Jiang, Y. Zhang, S. V. Dubonos, I. V. Grigorieva, and A. A. Firsov, Science **306**, 666 (2004).

[67] K. S. Novoselov, A. K. Geim, S. V Morozov, D. Jiang, M. I. Katsnelson, I. V Grigorieva, S. V Dubonos, and A. A. Firsov, Nature **438**, 197 (2005).

[68] A. H. Castro Neto, F. Guinea, N. M. R. Peres, K. S. Novoselov, and A. K. Geim, Rev. Mod. Phys. **81**, 109 (2009).

[69] C. R. Dean, A. F. Young, I. Meric, C. Lee, L. Wang, S. Sorgenfrei, K. Watanabe, T. Taniguchi, P. Kim, K. L. Shepard, and J. Hone, Nat. Nanotechnol. **5**, 722 (2010).

[70] C. R. Dean, A. F. Young, P. Cadden-Zimansky, L. Wang, H. Ren, K. Watanabe, T. Taniguchi, P. Kim, J. Hone, and K. L. Shepard, Nat. Phys. **7**, 693 (2011).

[71] C. R. Dean, L. Wang, P. Maher, C. Forsythe, F. Ghahari, Y. Gao, J. Katoch, M. Ishigami, P. Moon, M. Koshino, T. Taniguchi, K. Watanabe, K. L. Shepard, J. Hone, and P. Kim, Nature **497**, 598 (2013).

[72] J. M. Xue, J. Sanchez-Yamagishi, D. Bulmash, P. Jacquod, a Deshpande, K. Watanabe, T. Taniguchi, P. Jarillo-Herrero, and B. J. Leroy, Nat. Mater. **10**, 282 (2011).

[73] A. K. Geim and I. V. Grigorieva, Nature **499**, 419 (2013).

[74] T. Taychatanapat, K. Watanabe, T. Taniguchi, and P. Jarillo-Herrero, Nat. Phys. **7**, 621 (2011).

[75] T. Taychatanapat, K. Watanabe, T. Taniguchi, and P. Jarillo-Herrero, Nat. Phys. **9**, 225 (2013).

[76] A. F. Young, J. D. Sanchez-Yamagishi, B. Hunt, S. H. Choi, K. Watanabe, T. Taniguchi, R. C. Ashoori, and P. Jarillo-Herrero, Nature **505**, 528 (2014).

[77] L. Bretheau, J. I. J. Wang, R. Pisoni, K. Watanabe, T. Taniguchi, and P. Jarillo-Herrero, Nat. Phys. **13**, 756 (2017).

[78] V. E. Calado, S. Goswami, G. Nanda, M. Diez, a. R. Akhmerov, K. Watanabe, T. Taniguchi, T. M. Klapwijk, and L. M. K. Vandersypen, Nat. Nanotechnol. **10**, 761

(2015).

[79] M. Ben Shalom, M. J. Zhu, V. I. Fal'ko, A. Mishchenko, A. V. Kretinin, K. S. Novoselov, C. R. Woods, K. Watanabe, T. Taniguchi, A. K. Geim, and J. R. Prance, Nat. Phys. **12**, 318 (2016).

[80] H. B. Heersche, P. Jarillo-Herrero, J. B. Oostinga, L. M. K. Vandersypen, and A. F. Morpurgo, Nature **446**, 56 (2007).

[81] X. Du, I. Skachko, and E. Y. Andrei, Phys. Rev. B **77**, 184507 (2008).

[82] Ç. Girit, V. Bouchiat, O. Naaman, Y. Zhang, M. F. Crommie, a. Zettl, and I. Siddiqi, Nano Lett. **9**, 198 (2009).

[83] T. Dirks, T. L. Hughes, S. Lal, B. Uchoa, Y.-F. Chen, C. Chialvo, P. M. Goldbart, and N. Mason, Nat. Phys. **7**, 386 (2011).

[84] K. Komatsu, C. Li, S. Autier-Laurent, H. Bouchiat, and S. Guéron, Phys. Rev. B **86**, 115412 (2012).

[85] M. T. Allen, O. Shtanko, I. C. Fulga, J. I.-J. Wang, D. Nurgaliev, K. Watanabe, T. Taniguchi, A. R. Akhmerov, P. Jarillo-Herrero, L. S. Levitov, and A. Yacoby, ArXiv:1506.06734 (2015).

[86] D. K. Efetov, L. Wang, C. Handschin, K. B. Efetov, J. Shuang, R. Cava, T. Taniguchi, K. Watanabe, J. Hone, C. R. Dean, and P. Kim, (2015).

[87] F. D. Natterer, J. Ha, H. Baek, D. Zhang, W. G. Cullen, N. B. Zhitenev, Y. Kuk, and J. A. Stroscio, Phys. Rev. B **93**, 045406 (2016).

[88] F. Amet, C. T. Ke, I. V. Borzenets, J. Wang, K. Watanabe, T. Taniguchi, R. S. Deacon, M. Yamamoto, Y. Bomze, S. Tarucha, and G. Finkelstein, Science **352**, 966 (2016).

[89] H. Le Sueur, P. Joyez, H. Pothier, C. Urbina, and D. Esteve, Phys. Rev. Lett. **100**, 197002 (2008).

[90] J.-D. Pillet, C. H. L. Quay, P. Morfin, C. Bena, A. Levy Yeyati, and P. Joyez, Nat. Phys. **6**, 965 (2010).

[91] J.-D. Pillet, P. Joyez, R. Žitko, and M. F. Goffman, Phys. Rev. B **88**, 045101 (2013).

[92] W. Chang, V. E. Manucharyan, T. S. Jespersen, J. Nygård, and C. M. Marcus, Phys. Rev. Lett. **110**, 217005 (2013).

[93] J. Martin, N. Akerman, G. Ulbricht, T. Lohmann, J. H. Smet, K. von Klitzing, and a. Yacoby, Nat. Phys. **4**, 144 (2008).

[94] T. Dvir, M. Aprili, C. H. L. Quay, and H. Steinberg, Nano Lett. **18**, 7845 (2018).

[95] J. I.-J. Wang, L. Bretheau, D. Rodan-Legrain, R. Pisoni, K. Watanabe, T. Taniguchi, and P. Jarillo-Herrero, Phys. Rev. B **98**, 121411(R) (2018).

[96] S. Zihlmann, P. Makk, S. Castilla, J. Gramich, K. Thodkar, S. Caneva, R. Wang, S. Hofmann, and C. Schönenberger, Phys. Rev. B **99**, 1 (2019).

[97] T. Dvir, M. Aprili, C. H. L. Quay, and H. Steinberg, Phys. Rev. Lett. **123**, 217003 (2019).

[98] A. Zalic, S. Simon, S. Remennik, A. Vakahi, G. D. Gu, and H. Steinberg, Phys. Rev. B **100**, 64517 (2019).

[99] J. L. Davenport, Z. Ge, J. Liu, C. Nuñez-Lobato, S. Moon, Z. Lu, E. A. Quezada-Lopez, K. Hellier, P. G. Labarre, T. Taniguchi, K. Watanabe, S. Carter, A. P. Ramirez, D. Smirnov, and J. Velasco, Appl. Phys. Lett. **115**, (2019).

[100] N. Papadopoulos, P. Gehring, K. Watanabe, T. Taniguchi, H. S. J. Van Der Zant, and G. A. Steele, Phys. Rev. B **101**, 1 (2020).

[101] I. Keren, T. Dvir, A. Zalic, A. Iluz, D. LeBoeuf, K. Watanabe, T. Taniguchi, and H.

Steinberg, Nat. Commun. **11**, (2020).

[102] T. R. Devidas, I. Keren, and H. Steinberg, Nano Lett. **21**, 6931 (2021).

[103] L. Wang, I. Meric, P. Y. Huang, Q. Gao, Y. Gao, H. Tran, T. Taniguchi, K. Watanabe, L. M. Campos, D. A. Muller, J. Guo, P. Kim, J. Hone, K. L. Shepard, and C. R. Dean, Science **342**, 614 (2013).

[104] D. C. Ralph, C. T. Black, and M. Tinkham, Phys. Rev. Lett. **74**, 3241 (1995).

[105] C. T. Black, D. C. Ralph, and M. Tinkham, Phys. Rev. Lett. **76**, 688 (1996).

[106] A. Eichler, M. Weiss, S. Oberholzer, C. Schönenberger, A. Levy Yeyati, J. C. Cuevas, and A. Martín-Rodero, Phys. Rev. Lett. **99**, 126602 (2007).

[107] Y. J. Doh, S. De Franceschi, E. P. A. M. Bakkers, and L. P. Kouwenhoven, Nano Lett. **8**, 4098 (2008).

[108] C. B. Winkelmann, N. Roch, W. Wernsdorfer, V. Bouchiat, and F. Balestro, Nat. Phys. **5**, 876 (2009).

[109] F. Amet, J. R. Williams, A. G. F. Garcia, M. Yankowitz, K. Watanabe, T. Taniguchi, and D. Goldhaber-Gordon, Phys. Rev. B **85**, 073405 (2012).

[110] D. Halbertal, M. Ben Shalom, A. Uri, K. Bagani, A. Y. Meltzer, I. Marcus, Y. Myasoedov, J. Birkbeck, L. S. Levitov, A. K. Geim, and E. Zeldov, Science (80-.). **358**, 1303 (2017).

[111] V. Fatemi, S. Wu, Y. Cao, L. Bretheau, Q. D. Gibson, K. Watanabe, T. Taniguchi, R. J. Cava, and P. Jarillo-Herrero, Science **362**, 926 (2018).

[112] S. Wu, V. Fatemi, Q. D. Gibson, K. Watanabe, T. Taniguchi, R. J. Cava, and P. Jarillo-Herrero, Science (80-.). **359**, 76 (2018).

[113] J. I. Wang, D. Rodan-legrain, L. Bretheau, D. L. Campbell, B. Kannan, D. Kim, M. Kjaergaard, P. Krantz, G. O. Samach, F. Yan, J. L. Yoder, K. Watanabe, T. Taniguchi, T. P. Orlando, S. Gustavsson, P. Jarillo-herrero, and W. D. Oliver, Nat. Nanotechnol. **14**, 120 (2019).

[114] G. de Lange, B. van Heck, A. Bruno, D. J. van Woerkom, A. Geresdi, S. R. Plissard, E. P. A. M. Bakkers, A. R. Akhmerov, and L. DiCarlo, Phys. Rev. Lett. **115**, 127002 (2015).

[115] T. W. Larsen, K. D. Petersson, F. Kuemmeth, T. S. Jespersen, P. Krogstrup, J. Nygård, and C. M. Marcus, Phys. Rev. Lett. **115**, 127001 (2015).

[116] L. Casparis, T. W. Larsen, M. S. Olsen, F. Kuemmeth, P. Krogstrup, J. Nygård, K. D. Petersson, and C. M. Marcus, Phys. Rev. Lett. **116**, 150505 (2016).

[117] L. Casparis, M. R. Connolly, M. Kjaergaard, N. J. Pearson, A. Kringhøj, T. W. Larsen, F. Kuemmeth, T. Wang, C. Thomas, S. Gronin, G. C. Gardner, M. J. Manfra, C. M. Marcus, and K. D. Petersson, Nat. Nanotechnol. **13**, 915 (2018).

[118] A. Kringhøj, L. Casparis, M. Hell, T. W. Larsen, F. Kuemmeth, M. Leijnse, K. Flensberg, P. Krogstrup, J. Nygård, K. D. Petersson, and C. M. Marcus, Phys. Rev. B **97**, 1 (2018).

[119] D. I. Schuster, A. A. Houck, J. A. Schreier, A. Wallraff, J. M. Gambetta, A. Blais, L. Frunzio, J. Majer, B. Johnson, M. H. Devoret, S. M. Girvin, and R. J. Schoelkopf, Nature **445**, 515 (2007).

[120] A. A. Houck, D. I. Schuster, J. M. Gambetta, J. A. Schreier, B. R. Johnson, J. M. Chow, L. Frunzio, J. Majer, M. H. Devoret, S. M. Girvin, and R. J. Schoelkopf, Nature **449**, 328 (2007).

[121] J. A. Schreier, A. A. Houck, J. Koch, D. I. Schuster, B. R. Johnson, J. M. Chow, J. M. Gambetta, J. Majer, L. Frunzio, M. H. Devoret, S. M. Girvin, and R. J. Schoelkopf, Phys. Rev. B **77**, 180502 (2008).

[122] L. Bretheau, J. I.-J. Wang, R. Pisoni, K. Watanabe, T. Taniguchi, and P. Jarillo-Herrero, Nat. Phys. **13**, 756 (2017).

[123] V. Fatemi, A. R. Akhmerov, and L. Bretheau, Phys. Rev. Res. **013288**, 1 (2021).

[124] H. Weyl, Z. Phys **56**, 330 (1929).

[125] C. Herring, Phys. Rev. **52**, 365 (1937).

[126] S. Murakami, New J. Phys. **9**, (2007).

[127] X. Wan, A. M. Turner, A. Vishwanath, and S. Y. Savrasov, Phys. Rev. B - Condens. Matter Mater. Phys. **83**, 1 (2011).

[128] N. P. Armitage, E. J. Mele, and A. Vishwanath, Rev. Mod. Phys. **90**, 15001 (2018).

[129] B. Q. Lv, H. M. Weng, B. B. Fu, X. P. Wang, H. Miao, J. Ma, P. Richard, X. C. Huang, L. X. Zhao, G. F. Chen, Z. Fang, X. Dai, T. Qian, and H. Ding, Phys. Rev. X **5**, 031013 (2015).

[130] L. Lu, Z. Wang, D. Ye, L. Ran, L. Fu, J. D. Joannopoulos, and M. Soljačić, Science (80-.). **349**, 622 (2015).

[131] D. Z. Rocklin, B. G. G. Chen, M. Falk, V. Vitelli, and T. C. Lubensky, Phys. Rev. Lett. **116**, 1 (2016).

[132] X. Tan, Y. Zhao, Q. Liu, G. Xue, H. Yu, Z. D. Wang, and Y. Yu, Npj Quantum Mater. **2**, (2017).

[133] T. Zhang, Z. Song, A. Alexandradinata, H. Weng, C. Fang, L. Lu, and Z. Fang, Phys. Rev. Lett. **120**, 16401 (2018).

[134] W. J. Chen, M. Xiao, and C. T. Chan, Nat. Commun. **7**, 1 (2016).

[135] H. Jia, R. Zhang, W. Gao, Q. Guo, B. Yang, J. Hu, Y. Bi, Y. Xiang, C. Liu, and S. Zhang, Science (80-.). **363**, 148 (2019).

[136] R.-P. Riwar, M. Houzet, J. S. Meyer, and Y. V. Nazarov, Nat. Commun. **7**, 11167 (2015).

[137] S. Park, C. Metzger, L. Tosi, M. F. Goffman, C. Urbina, H. Pothier, and A. L. Yeyati, Phys. Rev. Lett. **125**, 077701 (2020).

[138] L. Peyruchat, J. Griesmar, J. D. Pillet, and Girit, Phys. Rev. Res. **3**, 1 (2021).

[139] V. Gritsev and A. Polkovnikov, Proc. Natl. Acad. Sci. U. S. A. **109**, 6457 (2012).

[140] M. D. Schroer, M. H. Kolodrubetz, W. F. Kindel, M. Sandberg, J. Gao, M. R. Vissers, D. P. Pappas, A. Polkovnikov, and K. W. Lehnert, Phys. Rev. Lett. **113**, 050402 (2014).

[141] P. Roushan, C. Neill, Y. Chen, M. Kolodrubetz, C. Quintana, N. Leung, M. Fang, R. Barends, B. Campbell, Z. Chen, B. Chiaro, A.Dunsworth, E. Jeffrey, J. Kelly, A.Megrant, J. Mutus, P. J. J.O'Malley, D. Sank, A. Vainsencher, J.Wenner, T. White, A. Polkovnikov, A. N. Cleland, and J. M. Martinis, Nature **515**, 241 (2014).

[142] Z. L. Xiang, S. Ashhab, J. Q. You, and F. Nori, Rev. Mod. Phys. **85**, 623 (2013).

[143] G. Kurizki, P. Bertet, Y. Kubo, K. Mølmer, D. Petrosyan, P. Rabl, and J. Schmiedmayer, Proc. Natl. Acad. Sci. **112**, 3866 (2015).

[144] A. A. Clerk, K. W. Lehnert, P. Bertet, J. R. Petta, and Y. Nakamura, Nat. Phys. **16**, 257 (2020).

[145] W. Chang, S. M. Albrecht, T. S. Jespersen, F. Kuemmeth, P. Krogstrup, J. Nygård, and C. M. Marcus, Nat. Nanotechnol. **10**, 232 (2015).

[146] S. M. Albrecht, A. P. Higginbotham, M. Madsen, F. Kuemmeth, T. S. Jespersen, J. Nyg, P. Krogstrup, and C. M. Marcus, Nature **531**, 206 (2016).

[147] J. Shabani, M. Kjaergaard, H. J. Suominen, Y. Kim, F. Nichele, K. Pakrouski, T. Stankevic, R. M. Lutchyn, P. Krogstrup, R. Feidenhans'l, S. Kraemer, C. Nayak, M. Troyer, C. M. Marcus, and C. J. Palmstrøm, Phys. Rev. B **93**, 155402 (2016).

[148] M. Hays, G. De Lange, K. Serniak, D. J. Van Woerkom, D. Bouman, P. Krogstrup, J. Nygård, A. Geresdi, and M. H. Devoret, Phys. Rev. Lett. **121**, 47001 (2018).

[149] L. Tosi, C. Metzger, M. F. Goffman, C. Urbina, H. Pothier, S. Park, A. L. Yeyati, J. Nygård, and P. Krogstrup, Phys. Rev. X **9**, 011010 (2019).

[150] M. Hays, V. Fatemi, K. Serniak, D. Bouman, S. Diamond, G. de Lange, P. Krogstrup, J. Nygård, A. Geresdi, and M. H. Devoret, Nat. Phys. **16**, 1103 (2020).

[151] M. Hays, V. Fatemi, D. Bouman, J. Cerrillo, S. Diamond, K. Serniak, T. Connolly, P. Krogstrup, J. Nygård, A. Levy Yeyati, A. Geresdi, and M. H. Devoret, Science (80-.). **373**, 430 (2021).

[152] A. Cheng, T. Taniguchi, K. Watanabe, P. Kim, and J. D. Pillet, Phys. Rev. Lett. **123**, 216804 (2019).

[153] X. M. H. Huang, R. Caldwell, L. Huang, S. C. Jun, M. Huang, M. Y. Sfeir, S. P. O'Brien, and J. Hone, Nano Lett. **5**, 1515 (2005).

[154] D. J. Van Woerkom, A. Proutski, B. Van Heck, D. Bouman, J. I. Väyrynen, L. I. Glazman, P. Krogstrup, J. Nygård, L. P. Kouwenhoven, and A. Geresdi, Nat. Phys. **13**, 876 (2017).

[155] J. Griesmar, R. H. Rodriguez, V. Benzoni, J. D. Pillet, J. L. Smirr, F. Lafont, and Girit, Phys. Rev. Res. **3**, 1 (2021).

[156] C. Rolland, A. Peugeot, S. Dambach, M. Westig, B. Kubala, Y. Mukharsky, C. Altimiras, H. Le Sueur, P. Joyez, D. Vion, P. Roche, D. Esteve, J. Ankerhold, and F. Portier, Phys. Rev. Lett. **122**, 186804 (2019).

[157] M. Steffen, S. Kumar, D. P. DiVincenzo, J. R. Rozen, G. A. Keefe, M. B. Rothwell, and M. B. Ketchen, Phys. Rev. Lett. **105**, 100502 (2010).

[158] A. Leggett, S. Chakravarty, A. Dorsey, M. P. A. Fisher, A. Garg, and W. Zwerger, Rev. Mod. Phys. **59**, 1 (1987).

[159] M. T. Bell, J. Paramanandam, L. B. Ioffe, and M. E. Gershenson, Phys. Rev. Lett. **112**, 167001 (2014).

[160] E. Majorana, Nuovo Cim. **14**, 171 (1937).

[161] M. T. Deng, S. Vaitiekenas, E. B. Hansen, J. Danon, M. Leijnse, K. Flensberg, J. Nygård, P. Krogstrup, and C. M. Marcus, Science (80-.). **354**, 1557 (2016).

[162] J. Klinovaja, M. J. Schmidt, B. Braunecker, and D. Loss, Phys. Rev. Lett. **106**, 1 (2011).

[163] J. Klinovaja, S. Gangadharaiah, and D. Loss, Phys. Rev. Lett. **108**, 1 (2012).

[164] U. C. Mendes and C. Mora, New J. Phys. **17**, 113014 (2015).

[165] U. C. Mendes, P. Joyez, B. Reulet, A. Blais, F. Portier, C. Mora, and C. Altimiras, **0**, 1 (2018).

[166] G. W. Deng, D. Wei, J. R. Johansson, M. L. Zhang, S. X. Li, H. O. Li, G. Cao, M. Xiao, T. Tu, G. C. Guo, H. W. Jiang, F. Nori, and G. P. Guo, Phys. Rev. Lett. **115**, 126804 (2015).

[167] J. D. Pillet, V. Benzoni, J. Griesmar, J. L. Smirr, and C. O. Girit, Nano Lett. **19**, 7138 (2019).